JGR Solid Earth

RESEARCH ARTICLE
10.1029/2024JB028714

A Century of Deformation and Stress Change on Kīlauea's Décollement

Lauren Ward Yong[1], James H. Foster[2,3], Bridget R. Smith-Konter[1], and L. Neil Frazer[1]

[1]Department of Earth Sciences, University of Hawai'i at Mānoa, Honolulu, Hawai'i, USA, [2]Hawai'i Institute of Geophysics and Planetology, University of Hawai'i at Mānoa, Honolulu, Hawai'i, USA, [3]Institute of Geodesy, University of Stuttgart, Stuttgart, Germany

Key Points:

- Collation of ~120 years of geodetic data at Kīlauea reveals key displacement, stress, and deformation source patterns throughout time
- Greater and more complex displacement occurred within Kīlauea's south flank prior to the 1975 M_W7.7 Kalapana earthquake than after it
- Compressive stress decreased in East Rift Zone before/after 1975; shear stress increased before and decreased after on Kīlauea décollement

Supporting Information:

Supporting Information may be found in the online version of this article.

Correspondence to:

L. W. Yong,
laward@hawaii.edu

Citation:

Yong, L. W., Foster, J. H., Smith-Konter, B. R., & Frazer, L. N. (2024). A century of deformation and stress change on Kīlauea's décollement. *Journal of Geophysical Research: Solid Earth*, *129*, e2024JB028714. https://doi.org/10.1029/2024JB028714

Received 10 JAN 2024
Accepted 5 NOV 2024

Author Contributions:

Conceptualization: James H. Foster, Bridget R. Smith-Konter
Formal analysis: Lauren Ward Yong, L. Neil Frazer
Funding acquisition: James H. Foster, Bridget R. Smith-Konter
Investigation: Lauren Ward Yong
Methodology: Lauren Ward Yong, James H. Foster, Bridget R. Smith-Konter, L. Neil Frazer
Project administration: James H. Foster
Resources: Lauren Ward Yong, James H. Foster
Software: Lauren Ward Yong
Supervision: James H. Foster, Bridget R. Smith-Konter
Validation: Lauren Ward Yong
Visualization: Lauren Ward Yong
Writing – original draft: Lauren Ward Yong
Writing – review & editing: Lauren Ward Yong

Abstract Kīlauea Volcano on Hawai'i Island is host to a complex volcanic and interwoven fault system. Over the last ~120 years, a range of seismic events, including large earthquakes such as the 1975 M_w7.7 Kalapana earthquake, creep, and slow slip events, have occurred along the décollement underlying Kilauea's south flank. We explore both the deformation and stress changes of Kīlauea from 1896 to 2018 by collating six geodetic data sets and creating an analytical model to determine the dominant deformation sources (i.e., fault planes, rifts, magma chambers) driving this system at different times. The 1975 Kalapana earthquake significantly altered the region's state of stress and deformation; we find the average slip along the décollement was reduced from 10 cm/yr prior, to 4 cm/yr after the rupture. Prior to 1975 no slip is resolved along the décollement where the earthquake nucleated, suggesting that this portion may have been locked leading up to the rupture. After 1975, décollement slip overall is smaller and more irregular, suggesting increased control by spatial variation of mechanical properties. We find increases in shear stress along the Kīlauea décollement and a decrease in normal compressive stress within the East Rift Zone prior to the Kalapana earthquake, creating favorable conditions for failure of the décollement and subsequent magmatic intrusion.

Plain Language Summary Kīlauea Volcano on Hawai'i Island encompasses a complex volcanic and interwoven fault system. The low-angle fault underlying the volcano has consistently been moving it southward, and has a high hazard potential due to large magnitude earthquakes. The complexity of this region leads to questions about the evolution of deformation and its seismic cycle. The 1975 M_w7.7 Kalapana décollement earthquake is of particular interest because large magnitude ruptures can dramatically alter the state of stress within a region. We therefore explore both the deformation and stress changes of Kīlauea's décollement from 1898 to 2018 by collating a wealth of surface displacement observations. We create a model to reproduce the observed displacements throughout time and to identify key structural features causing the deformation, such as fault planes, rifts, and magma chambers. Multiple deformation sources were needed to model the observations, with more of these sources required prior to the 1975 Kalapana earthquake than afterward. We also find varied patterns and magnitudes of deformation and stress both temporally and spatially within the region. Kīlauea's history has important implications for our understanding of the relationship between magmatic and earthquake cycle processes.

1. Introduction

Hawai'i Island was formed by the growth of five major shield volcanoes, two of which, Mauna Loa and Kīlauea, are still active. The complexity and interactions of these volcanoes have resulted in a wide range of magmatic and seismic activity (Atkinson, 2010; McNamara et al., 2020). For example, the 29 November 1975 M_w7.7 Kalapana earthquake, which occurred along the south flank of Kīlauea volcano near the coastline (Figure 1), generated an average total slip of 7.9 m and an average vertical slip of 0.91 m (Nettles & Ekström, 2004). This devastating event also resulted in a large tsunami (maximum wave height of 14.6 m) that hit the southeast shore of the island, causing significant damage and two fatalities (Ma et al., 1999). In addition to large earthquakes, micro-seismicity and slow slip events (SSEs) have been found to contribute to the region's seismic cycle (e.g., Brooks et al., 2008; Foster et al., 2013; Lin et al., 2020; Montgomery-Brown et al., 2010; Wolfe et al., 2007), and in the past ~20 years a consistent southward displacement of ~6 cm/yr has been observed along Kīlauea's south flank (e.g., Delaney & Denlinger, 1999; Miklius et al., 2005).

The seismic evolution of these volcanic systems is also related to a complex sequence of magmatic intrusion, storage, and eruption at the Earth's surface (Yin & Kelty, 2000). Early work by Swanson et al. (1976) proposed

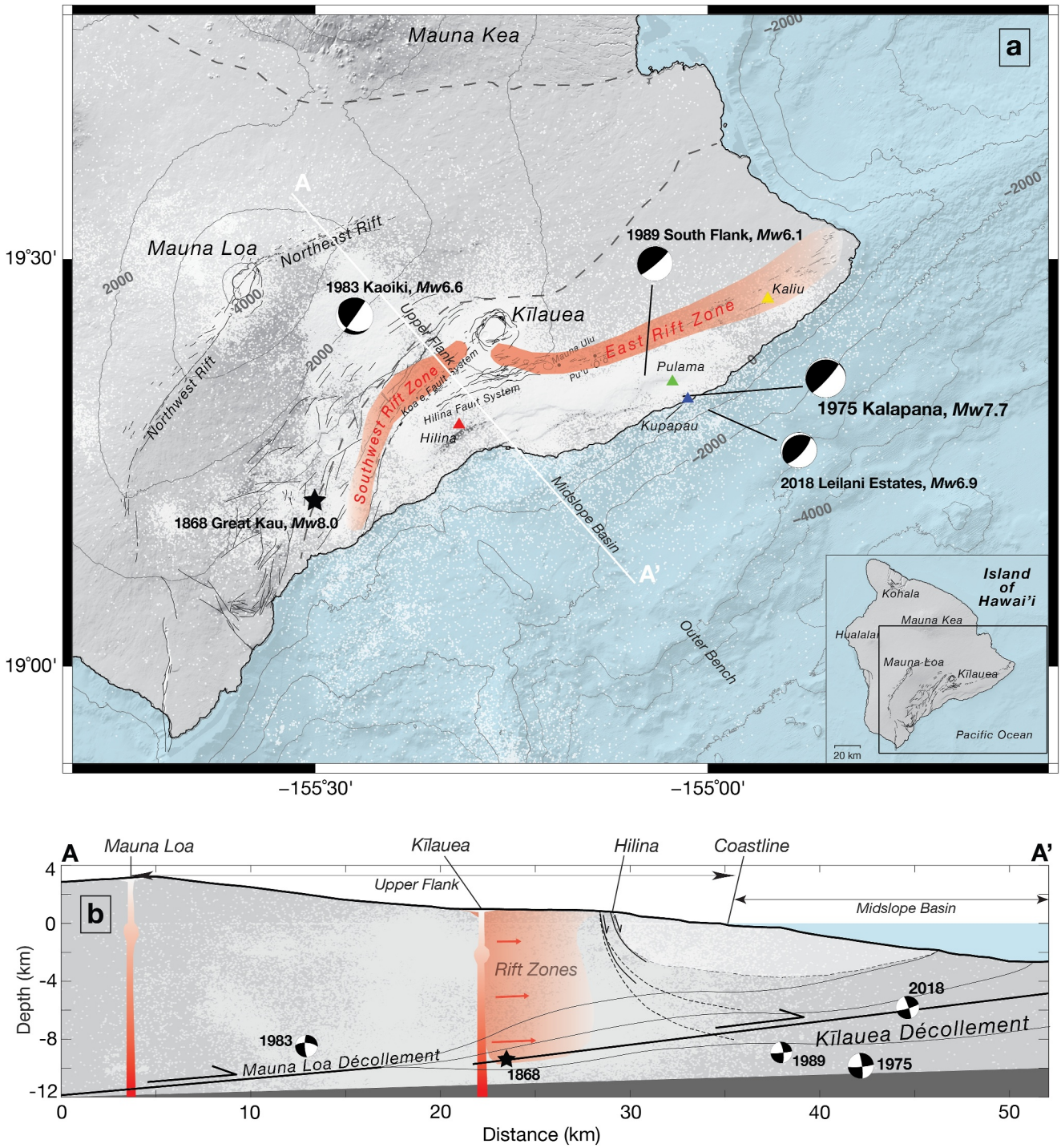

Figure 1.

that increased pressure from forceful dike intrusion into the rift zones could displace the south flank of Kīlauea volcano seaward. Lipman et al. (1985) suggested that inflation of Mauna Loa volcano to the north, resulting in a July 1975 summit eruption, may have contributed to the destabilization of Kīlauea's south flank and triggering of the earthquake. More recent work (e.g., Borgia et al., 2000; Morgan et al., 2003; Phillips et al., 2008) suggests that the inherent gravitational instability caused by the topography of Kīlauea's south flank, also contributes to the observed southward displacement of the region, resulting in both secular motion and catastrophic failure, like that of the 1975 Kalapana earthquake.

Deformation from these volcanoes has been heavily monitored by geologic and geophysical observations dating back to the 19th century (e.g., Swanson et al., 1976; Wright & Klein, 2014; Wyss, 1988), and in more recent (~40) years the modeling of these observations has led to a better understanding of the hazards associated with Mauna Loa and Kīlauea. Various deformation sources have been inferred from such deformation observations (e.g., Arnadottir et al., 1991; Baker & Amelung, 2015; Crosson & Endo, 1981; Hooper et al., 2002; Segall et al., 2001; Wu et al., 2021). Specifically, these deformation sources include: (a) low-angle, thrusting detachment faults between the base of the volcanic edifices and the pre-Mauna Loa seafloor (décollements), (b) opening and contracting magmatic rift zones and subsequent surface faults, (c) high-angle normal faults caused by gravitational instability from the weight of the volcanic island on the crust and upper mantle, and (d) inflation and deflation of magmatic chambers/conduits from the movement of magma beneath the surface. Thrust faulting, however, is responsible for most (~80%) of the seismic energy released (Gillard, Rubin, & Okubo, 1996), particularly deep within the flank, while normal faulting dominates the shallower portions of the crust (Yin & Kelty, 2000).

Similar deformation mechanisms may have also contributed to several other ~M_w6 earthquakes, such as the 2018 M_w6.9 earthquake (Liu et al., 2018; Neal et al., 2019), the 1989 M_w6.1 earthquake along Kīlauea's décollement near the East Rift Zone (Arnadottir et al., 1991; Hooper et al., 2002), and the 1983 M_w6.6 earthquake along the Kaoiki fault system near the Southwest Rift Zone (Okubo et al., 1997). Furthermore, in 1868, the ~M_w8 Great Ka‘ū earthquake caused slip along Kīlauea's décollement, and is considered to be a large Kalapana-like earthquake (Wyss, 1988). Other recent major events include the 1977 eruption within the East Rift Zone (Delaney et al., 1992; Lipman et al., 1985), which was followed by the Pu‘u ‘Ō‘ō eruption that started in the East Rift Zone in 1983 (Gillard, Wyss, & Okubo, 1996) and persisted for over 35 years (Garcia et al., 2021). These events (and many others, see Table S1 in Supporting Information S1) demonstrate that abundant, complex, deformation occurs within this region, as well as along Kīlauea's décollement, creating both seismic and volcanic hazards. The connections and interactions of these deformation sources and processes are fundamental for our understanding of natural hazards throughout Hawai'i.

While many previous studies have considered a single type of geodetic data set, specific time period, or sole event to investigate deformation sources within the seismically and magmatically active regions of Hawai'i Island, this study considers deformation observations within the broad southeast Mauna Loa and Kīlauea region (18.9°–19.8°N, 154.6–155.8°W) from several types of geodetic data over the past 122 years. Although it is a sequence of individual events whose cumulative effects generate the long-term deformation signals, focusing on these individual events runs the risk of losing sight of the big picture in the details of the complex interactions between these events. Instead, our goal is to determine the combinations of deformation sources necessary to describe broad patterns of displacement and stress through three specific epochs during this period, and examine any

Figure 1. (a) Regional map of the southeast portion of the Big Island of Hawai'i with elevation and bathymetry contours and surface fault traces. Thick gray dashed lines show approximate perimeters of Mauna Kea, Mauna Loa, and Kīlauea volcanic regions. White dots denote locations of seismicity from 1933 to 2018 (see Section 2 for data details). Triangles mark key observation locations shown with their time series in Figure 12. The approximate location of the ~M_w8 1868 Great Ka‘ū earthquake (Wyss, 1988) is indicated by a star; and Centroid-Moment-Tensor (CMT) solutions (from www.globalcmt.org: Dziewonski et al., 1981; Ekström et al., 2012) are plotted at the epicenters of the M_w7.7 1975 Kalapana earthquake (Nettles & Ekström, 2004), the M_w6.6 1983 Kaoiki earthquake, the M_w6.1 1989 south flank earthquake, and the M_w6.9 2018 earthquake. Inset figure shows a full map of the Big Island of Hawai'i and the five major volcanoes that comprise the island. (b) Cross-section of the A-A′ profile shown on (a) and approximate projected locations of key geologic features. Note that due to the coast line being oblique to perpendicular to the cross-section the major earthquakes appear further offshore in this perspective than is actually the case. The orientations and southward direction of motion is shown for the décollements below Mauna Loa and Kīlauea volcanoes and the Hilina Fault System (whose extent and orientation is poorly constrained, and we do not find necessary as an element in our modeling). Estimated (southwest and east) rift zones and summit magma chamber/conduit locations are illustrated in red. White dots indicate seismicity locations at depth from 1933 to 2018 within 10 km on either side of the A-A′ profile. Kīlauea's decollement is shown here at the depth found from the analysis of our geodetic data. It is almost certainly deeper: see text for discussion.

differences between them. We collated geodetic data observations from 1896 to 2018 from six different geodetic data sets that include five different types of observations: triangulation, EDM, leveling, Global Navigation Satellite System (GNSS), and offshore pressure sensor (PS) data. As the 1975 Kalapana earthquake was the single most significant event during this time, we divide our analysis into three distinct time periods: (a) 1896–1974, prior to the 1975 Kalapana earthquake of 29 November 1975; (b) 1975, encompassing the Kalapana M_w7.7 earthquake, and ranging from 26 June 1974 to 21 May 1976 in order to include observations immediately prior to and after the earthquake for a majority of the stations within our data sets; (c) 1976–2018, after the 1975 Kalapana earthquake, which includes all observations following 29 January 1976 (1 month after the earthquake) to avoid any afterslip or large magnitude displacements that may have occurred shortly after the rupture and that would affect the long-term displacement rates we are trying to resolve.

Based on these observations and previous modeling efforts (e.g., Arnadottir et al., 1991; Baker & Amelung, 2015; Delaney & Denlinger, 1999; Delaney et al., 1998; Hooper et al., 2002; Montgomery-Brown et al., 2009; Owen, Segall, Lisowski, Miklius, Murray, et al., 2000; Owen, Segall, Lisowski, Miklius, Denlinger, & Sako, 2000; Phillips et al., 2008; Segall et al., 2001; Shirzaei et al., 2013), we developed an analytical deformation model comprised of 15 candidate deformation sources: 11 fault planes that accommodate either décollement thrusting, or strike-slip and/or tensile motions along rift zone dislocations (Okada, 1985), and four inflation/deflation magmatic sources that accommodate the influx or drainage of magma, simulated by point sources of volume change (Mogi, 1958). Green's functions were used to invert the deformation observations for optimal slip rates or volume changes for each model source. A 5-fold cross-validation technique was then used to find the optimal combination of sources for each of the three time periods. Geometry parameter values (such as strike, dip, and depth) of the sources were specified a priori and adjusted later using an approximate profile likelihood procedure, where possible. Forward models were then run for each time period's optimal model configuration to estimate displacements. Lastly, we estimated Coulomb and rift-normal stress changes for each time period based on our modeled slip and volume change rates (or modeled rate parameters), and considered the implications for the 1975 M_w7.7 Kalapana earthquake as well as the more recent 2018 M_w6.9 earthquake.

2. Data

We used over 15,000 displacement observations from 1896 to 2018 that span the broad Mauna Loa and Kīlauea regions, including horizontal displacements resulting from 1896 to 1970 triangulation and trilateration surveys (Swanson et al., 1976), changes in baseline lengths (or range) from 1970 to 1995 electronic distance measurements (EDM), changes in height from 1963 to 2012 leveling campaigns, GNSS campaign observations from 1990 to 1996 (Owen, Segall, Lisowski, Miklius, Murray, et al., 2000) and continuous GNSS observations from 1996 to 2018, as well as vertical offshore PS displacements from 2000 to 2004 (Phillips et al., 2008). A major component of this study therefore involved collating multiple types of geodetic data into a compatible and comparable format and making this data compilation accessible to the scientific community. Each geodetic data set (and its errors) was converted into displacement rates (cm/yr) spanning the three time periods of this analysis (before, during, and after the 1975 Kalapana earthquake). A detailed description of each data set is provided next, and data files with our estimated displacement rates for each observation type are provided as supporting files for each time period. We also provide seismicity data spanning 1933–2018, including data available for 1986–2018 from a high-precision relocation of seismicity study (Matoza et al., 2021), 1960–2016 from the Northern California Earthquake Data Center Hawai'i Earthquake Catalog (NCEDC, 2014), and for 1933–1959 from Klein and Wright (2000). That supporting file contains 338,396 earthquake observations with their location, depth, and magnitude.

2.1. 1896–1970 Triangulation and Trilateration Vectors

The earliest observations utilized in this study are horizontal displacements derived from regional control surveys reported by Swanson et al. (1976), which all predate the 1975 M_w7.7 Kalapana earthquake. These observations span Kīlauea's summit, the east and southwest rift zones, and the Hilina fault system (19.1°–19.7°N, 154.7–155.5°W, see Figure 1). The earlier surveys are triangulations (1896 and 1949 by the U.S. Coast and Geodetic Survey, 1958 and 1961 by the U.S. Geological Survey). The more recent survey, in 1970, by the Hawaiian Volcano Observatory (HVO) using trilateration. A total of 43 stations were surveyed, and the horizontal displacements were reported as the total observed displacements over the times between the surveys (9–62 years). We converted these to horizontal displacement rates (cm/yr) for each station within its survey time period. If a station was occupied multiple times throughout the full time period of the data set (e.g., 1896–1970), we took the

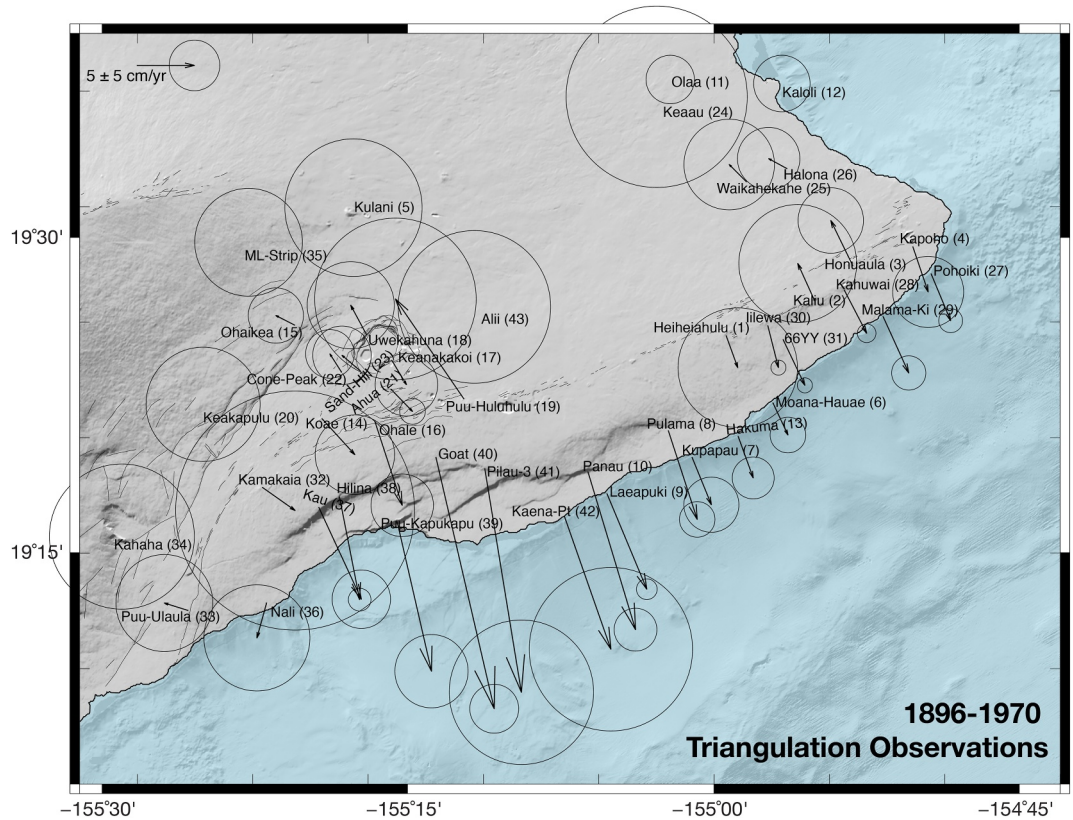

Figure 2. Horizontal displacement rates from 1896 to 1970 derived from triangulation and trilateration surveys of Swanson et al. (1976). Unique station identification numbers are also shown in parentheses next to their names. Station positions, rates, and errors for all 43 stations can be found in our supporting data files. Stations without arrows have zero velocity with large uncertainty.

average of the horizontal displacement rates at the station. Using displacement rates (Figure 2) allowed us to compare directly with the other types of geodetic data analyzed throughout this study. The errors of each observation (Swanson et al., 1976) were also converted into cm/yr rates (plotted as ellipses in Figure 2). Large error rates are partially due to the uncertainty in the stability of the control stations north of Kīlauea's summit that spanned multiple different surveys throughout the years. Uncertainties in the orientation of the horizontal displacement vectors also arise from problems of imprecision and the sub-optimal geometry of the survey networks. Although these data have their shortcomings (see Swanson et al., 1976), they reveal the early, long-term deformation trends of Kīlauea prior to the 1975 Kalapana earthquake. Specifically, we note the general southward displacement of Kīlauea's south flank, as well as rift-opening deformation along the East Rift Zone and on either side of Kīlauea's summit. Coastal stations reveal large southward motion while inland stations show small magnitude northward motion.

2.2. 1970–1995 Electronic Distance Measurements

Electronic distance measurements (EDM) were carried out by the HVO from 1970 to 1995 (Decker et al., 2008; Hanatani, 1987), spanning the 1975 M_w7.7 Kalapana earthquake. This data set contains 1,917 observations of the baseline distance between a source and target station (station pair).

There are a total of 90 stations in this data set, and 228 station pairs were utilized to create a geometric network that spans a region of 19.1°–19.8°N and 154.7–155.5°W (Figure 3), extending farther north than the previous triangulation and trilateration data sets. Within each of our three analyzed time periods (before, during, and after the Kalapana earthquake), and for every station pair with more than one observation, the first recorded range was subtracted from the last recorded range and divided by the time between the observations to give the displacement rate (cm/yr) for each station pair for all three time periods. Displacement rate errors were determined by combining

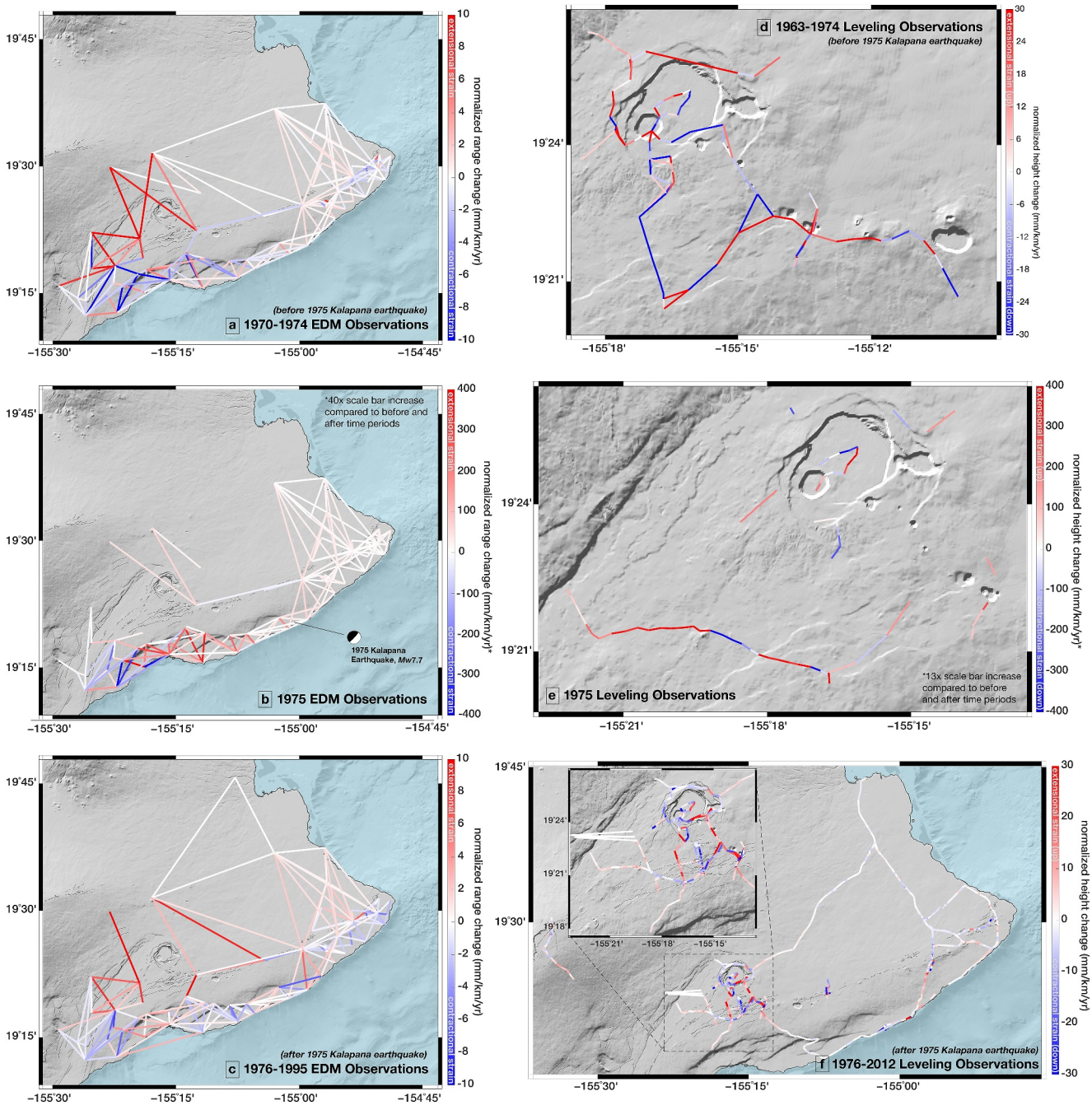

Figure 3. Electronic distance measurement (EDM) normalized baseline displacement rates (i.e., strain rates) from 1970 to 1995 provided by the Hawaiian Volcano Observatory (HVO) courtesy of A. Miklius and I. Johanson. EDM observations were recorded by 90 different stations and were separated into three time periods surrounding the 1975 Kalapana earthquake: (a) 1970–1974 (before the rupture), (b) 1975 (encompassing the M_w7.7 rupture), and (c) 1976–1995 (after the rupture). Station positions, rates, and errors from source and target station pairs can be found in our supporting data files. Leveling observations (normalized height change, or strain rate) and associated error from 1963 to 2012 provided by the HVO courtesy of A. Miklius and I. Johanson. Observations were recorded by 919 different stations and were separated into three time periods surrounding the 1975 Kalapana earthquake: (d) 1963–1974 (before the rupture), (e) 1975 (encompassing the M_w7.7 rupture), and (f) 1976–2012 (after the rupture). The specific location, rates, and errors for all observations from source and target station pairs can be found in our supporting data files.

the errors for the first and last reported range observation and dividing by the time between those observations. Any observations with errors greater than 5 cm/yr were excluded from the data set; we chose this inclusion threshold due to the age of the data set and the potential transcriptional and estimation errors that may have occurred during the several different campaigns. These errors reflect overall process errors in addition to individual observation errors,

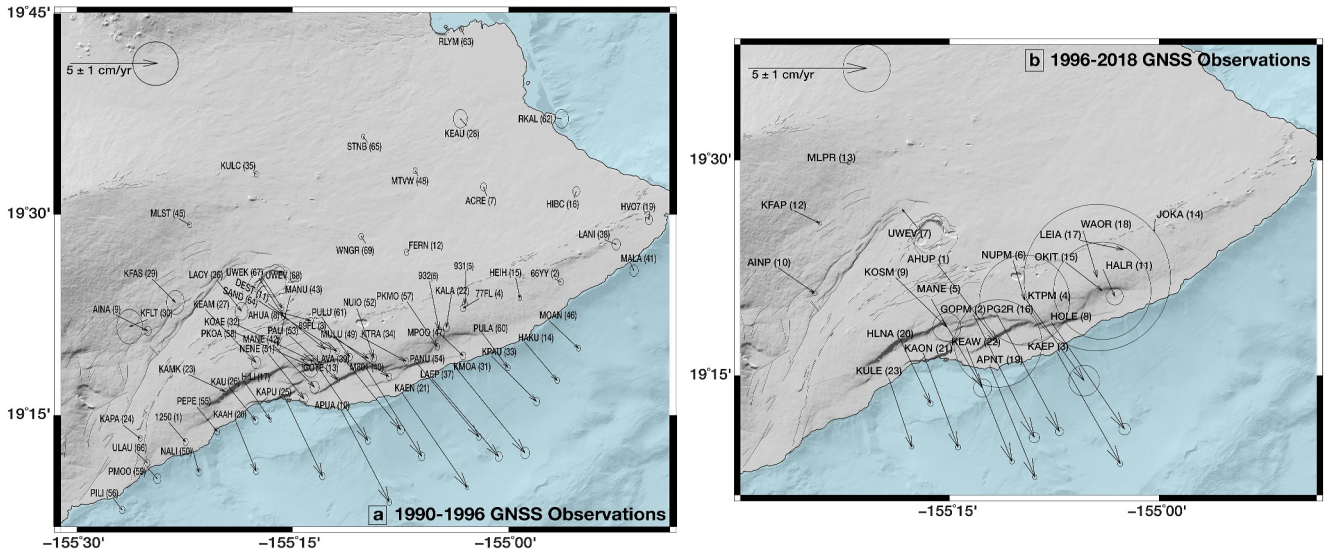

Figure 4. (a) 1990–1996 campaign Global Navigation Satellite System (GNSS) horizontal observations (69 stations) reported in Owen, Segall, Lisowski, Miklius, Murray, et al. (2000). (b) 1996–2018 continuous GNSS horizontal observations (23 stations) from our own solutions using University of Hawaii and Hawaiian Volcano Observatory data. Large errors, mainly located in the East Rift Zone, within this data set can be attributed to multiple discrete event offsets (e.g., rapid and complex inflation and deflation relating to local magma storage and transport) that occurred there during this time period. Unique station identification numbers are shown in parentheses next to their names. Station positions, rates, and errors for all observations from both GNSS data sets can be found in our supporting data files.

as displacements were determined based on the full geodetic network. For plotting purposes, we divided the EDM displacement rates by the length of the baseline (km) (Figure 3), to arrive at strain rates (mm/km/yr); thus short baseline observations with large changes in range represent high strain rate, while long baseline observations with large changes in range represent modest strain rate. Our sign convention is that extensional strain rate, or baseline lengthening, is positive (red) and contractional strain, or baseline shortening, is negative (blue).

The strain rates reveal changes in distance and motion between the stations, and vary considerably over the three time periods of this analysis. Over the 5 years leading up to the Kalapana earthquake (1970–1974, Figure 3a), large southward motion was heavily focused on the southwest portion of the flank. The largest (>40 mm/km/yr) extensional rates (red) were across Kīlauea's summit and the Southwest Rift Zone. The largest contractional rate (blue) occurred also on the western edge of our field area from the coastline to the top of the Hilina Fault system. The rest of the contractional rates are located mainly along the coast below the East Rift Zone (e.g., Swanson et al., 1976; Thurber & Gripp, 1988). Conversely, the eastern portion of the EDM network remained close to stable throughout time period. Deformation from the 1975 Kalapana earthquake (Figure 3b), reveals a very different pattern of strain, greater by an order of magnitude, with a maximum 930 ± 5 mm/km/yr (~1 m of extension per year) spanning the Hilina fault system. Post-earthquake deformation, in the time period of 1976–1995 (Figure 3c), shows lower magnitude displacements than those leading up to the earthquake (1970–1974), with extension (red) now occurring east of Kīlauea's summit as well. The largest extensional rate occurred directly south of Kīlauea summit and across the eastern portion of the Hilina fault system (10 ± 4 mm/km/yr), while the largest contractional rates occurred near the coast and epicenter of the 1975 earthquake (−12 ± 1 mm/km/yr). Overall, regional displacement after 1975 is more heterogeneous than prior to the Kalapana earthquake, and the errors are smaller due to the increased number of observations and the improvement in measurement accuracy.

2.3. 1963–2012 Leveling Data

HVO collected 13,330 leveling observations from 919 stations spanning 49 years (1963–2012). We compiled these to establish a geometric network of 1,737 station pairs and to estimate the height change of each element of the pair (Figure 3). Similar to the EDM data set, for each of the three time periods (before, during, and after the Kalapana earthquake), for every station pair with more than one observation, the first recorded height was removed from the last recorded height and divided by the time between the observations to obtain a displacement rate (cm/yr). Displacement rate errors were determined by combining the error for the reported first and last height observation and dividing by the time between the observations. As in our treatment of the EDM, any

leveling observations with errors greater than 5 cm/yr were excluded from the data set. These errors reflect overall process errors in addition to individual observation errors because, as in the EDM data set, displacements were determined based on the full geodetic network. For plotting purposes and easier comparison to the EDM, we divided displacement rates by the length of the baseline (km) to display strain rates (mm/km/yr) (Figure 4). Similar to the EDM data, we adopt a sign convention where extensional strain rate relates to a positive (red) change in height between stations (relative uplift) and contractional strain relates to a negative (blue) change in height (relative subsidence).

The leveling data set spans a geographic region similar to the EDM data set except that, for the time periods before and during the 1975 Kalapana earthquake, observations were limited to a smaller region surrounding the summit of Kīlauea. The distances between station pairs are significantly smaller than those of the EDM network - generally less than 0.5 km. The leveling observations reveal relative vertical displacements, highlighting more the local-scale deformation that occurred over the time between campaigns rather than the motion of the entire region. We incorporated this data set to better constrain the deformation of Kīlauea's summit, which we and several previous studies find to be a key source of deformation for the region because of the movement of magma within its chambers and connected conduits beneath the surface (e.g., Chen et al., 2019; Delaney et al., 1998; Morgan, 2006; Owen, Segall, Lisowski, Miklius, Murray, et al., 2000).

Throughout each of the three time periods, significant variations in leveling height surround the summit of Kīlauea, revealing heterogeneous patterns of displacements. These variations are generally tied to the inflation-deflation cycles that occur due to the movement of magma into and out of Kīlauea's magma chamber/conduits beneath the surface. Inflation or intrusion of magma below the summit generally results in uplift and extension away from the summit center on the surface, while deflation or depletion of magma below the summit results in subsidence and contraction toward the summit center on the surface (e.g., Johnson, 1987, 1992; Mogi, 1958). Before the 1975 Kalapana earthquake (Figure 4a), the greatest increase in the rate of height change, 1,174 ± 17 mm/km/yr (~1 m of uplift per year between the station pair), was measured across the northern edge of the summit, while the greatest rate of height decrease, −2,067 ± 8 mm/km/yr (~2 m of subsidence per year between the station pair), occurred south of the summit. These reflect displacements across local faults, and overall heterogenous height changes are seen throughout the area. During the 1975 Kalapana earthquake period (Figure 3e), again a combination of uplift and subsidence were observed surrounding the summit with a complex displacement pattern. A maximum uplift rate of 7,976 ± 172 mm/km/yr and a maximum subsidence rate of −5,978 ± 106 mm/km/yr were recorded. This increased magnitude of height changes is due to the eruptions that occurred at the Kīlauea summit and along the Southwest Rift Zone during this time period, as well as the observations' proximity to the Hilina fault system where a majority of both horizontal and vertical displacement occurred during the earthquake (e.g., Lipman et al., 1985). After the 1975 Kalapana earthquake (Figure 3f), the northern edge and overall area of the summit subsided by as much as −4,573 ± 2 mm/km/yr, while the southern edge locally uplifted by at most 3,963 ± 2 mm/km/yr. This contrasts with the time period before the earthquake and from the typical inflation-deflation cycles that previously controlled the summit. These changes and the increased complexity of deformation patterns, where the majority of the region surrounding Kīlauea's summit has been subsiding since the earthquake, have also been reported by previous studies (e.g., Delaney et al., 1992, 1998; Lipman et al., 1985; Miklius et al., 2005; Owen, Segall, Lisowski, Miklius, Murray, et al., 2000), and result mainly from the large seaward displacement of the south flank. The remainder of the height change observations outside of the summit region remained largely stable for the period after the Kalapana earthquake.

2.4. 1990–2018 GNSS Vectors

Two different GNSS data sets were incorporated in this study. The first data set (GNSS-1) observed deformation from 1990 to 1996 and was provided by Owen, Segall, Lisowski, Miklius, Murray, et al. (2000). Campaigns measuring 69 GNSS stations were processed and reported as north and east components of displacement rate in cm/yr (Figure 4a). These stations cover a similar region of interest (19.1°–19.8°N, 154.8–155.5°W) and provide the highest accuracy observations with errors ranging from 0.06 to 0.59 cm/yr. Notably, the deformation during this time period exhibited steady displacement rates, simplifying station velocity estimates and helping to minimize their uncertainty. The majority of GNSS-1 displacement rates show southward motion of Kīlauea's south flank with a maximum of 7.04 ± 0.08 cm/yr at station KAEN. There is also low magnitude northward motion on the northern side of the East Rift Zone, with a maximum displacement rate of 0.60 ± 0.39 cm/yr at station KEAU.

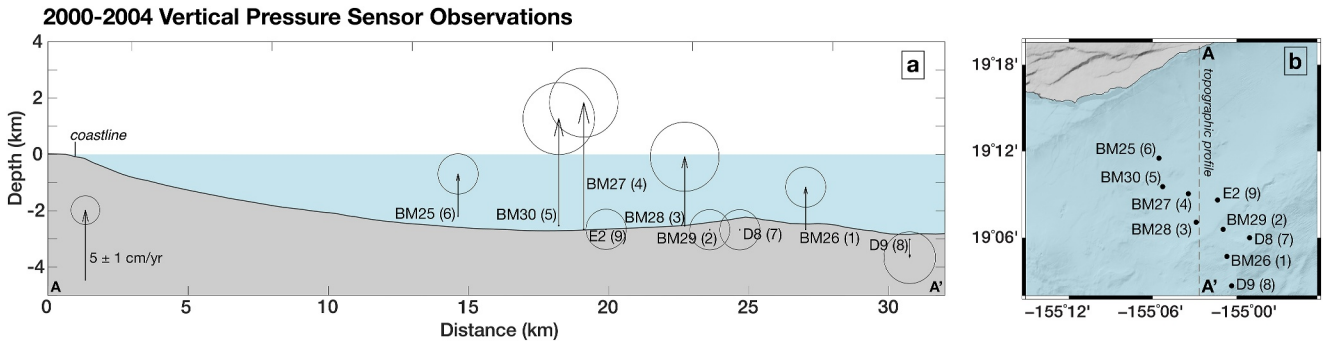

Figure 5. (a) 2000–2004 vertical displacements at depth determined by offshore pressure sensors (Phillips et al., 2008). The bathymetric profile that runs north-south along the center of the observation region is shown in map view in (b). Unique station identification numbers are shown in parentheses next to their names. The bathymetry was extracted from 50 m resolution grids available at http://www.soest.hawaii.edu/hmrg/multibeam/index.php. (b) Map view of the 9 station locations, south and offshore from Kīlauea, Hawai'i. Positions, rates, and errors for all observations for this data set can be found in our supporting data files, as well as in Phillips et al. (2008).

The second GNSS data set (GNSS-2) is comprised of 23 continuous stations, covers a smaller region (19.1°–19.6°N, 154.8–155.5°W), and is the most up to date data set considered by this study (Figure 5b). It does not extend as far north or east as the previous 1990–1996 campaign GNSS data set, but it captures key regions such as Kīlauea's summit, the Hilina fault system, and a large portion of the East Rift Zone. All stations exhibit southward motion except for station UWEV just north of Kīlauea's summit. The largest southward displacement rate occurs at station GOPM within the Hilina region at 5.80 ± 0.22 cm/yr. There are, however, seven stations that have errors >1 cm/yr, which reside in the highly active area of the East Rift Zone. The long-term motion of these sites is not well represented by a single velocity due to discrete event offsets that have occurred here. These stations instead record periods of rapid and complex inflation and deflation relating to local magma storage and transport. As a result, the formal errors of the fits of the long-term velocities to their displacement time-series are very high. Despite some large uncertainties within the GNSS-2 data set, we incorporate it into our study to represent modern displacement observed within the Kīlauea region.

2.5. 2000–2004 Vertical Offshore PS Data

Vertical displacements from offshore PS observations from 2000 to 2004 were also included in this study (Phillips et al., 2008). There are nine stations each with a single vertical displacement rate (Figure 5). This data set provides critical constraints on the far-field deformation of Kīlauea's décollement, which is known to extend offshore (e.g., Denlinger & Okubo, 1995; Liu et al., 2018; Morgan et al., 2000; Owen, Segall, Lisowski, Miklius, Murray, et al., 2000). The PS data are positioned along a transect south of Kīlauea's summit, stretching as far offshore as the outer bench (Figure 1b). A maximum of 9.0 ± 2.4 cm/yr of uplift was found at station BM27, located around the center of the observation region (19.0°–19.3°N, 154.9–155.3°W) in the midslope basin. All other stations either remained stable or recorded uplift, except the southernmost observation (station D9), which observed a subsidence rate of 1.3 ± 1.8 cm/yr. This PS data set and the leveling data set are the only data sets considered here that depict vertical displacements.

3. Analytical Model

3.1. Model Construction

To reproduce the observed deformation from these six geodetic data sets and to understand the dominant deformation sources driving this system, we developed a 3D analytical deformation model characterized by dislocations (Okada, 1985) and point sources of volume change (Mogi, 1958) within a homogeneous elastic half-space. Although we take into account the site elevations when calculating the Green's functions for our observation locations, we do not include a topographic correction as the slopes for Kilauea and Mauna Loa are low (e.g., Cayol & Cornet, 1998). Fifteen possible sources (Figure 7) were considered based on models from earlier studies (mainly Owen, Segall, Lisowski, Miklius, Murray, et al., 2000) that mapped fault surface traces, and/or documented seismic and magmatic events within the region. A list of the events considered when creating our model can be found in Table S1 in Supporting Information S1. The dates of the major events that occurred at, or

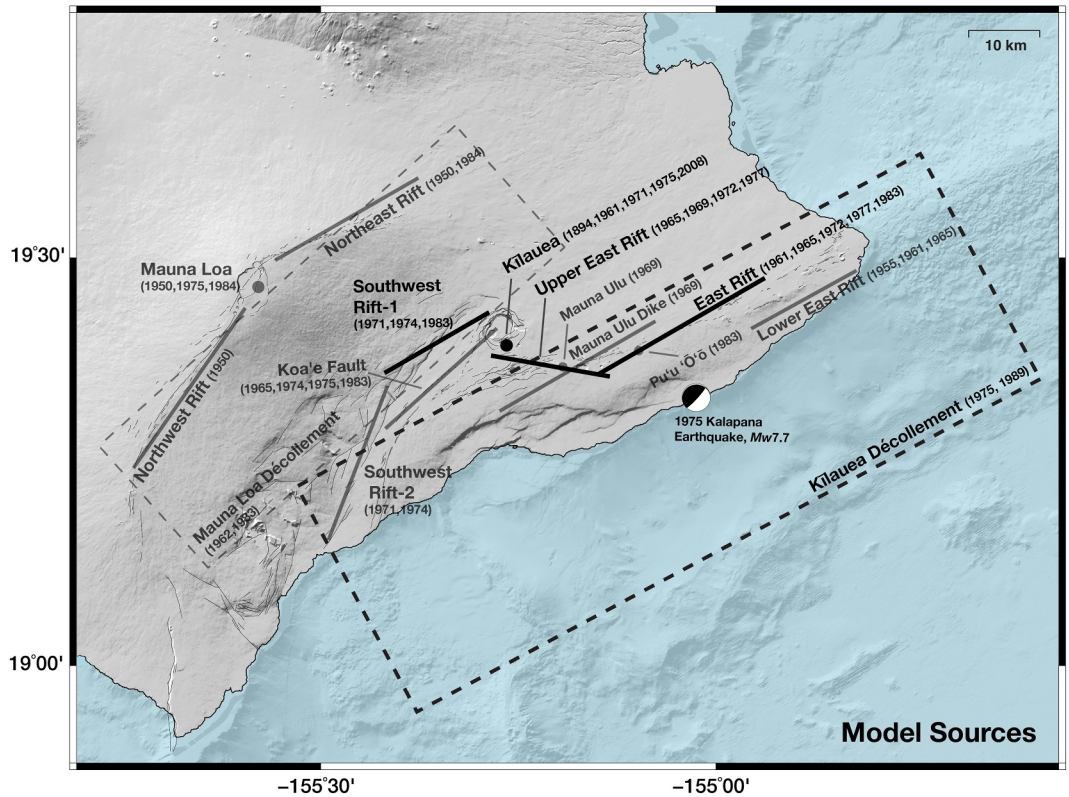

Figure 6. Full catalog of model deformation sources used to reproduce observed displacements from the 6 geodetic data sets spanning 1896–2018 within the southeast Mauna Loa and Kīlauea region of Hawai'i Island. Dates of some of the major events that occurred at, or impacted, the deformation sources are also noted. There are 15 possible model sources, which include two low-angle decollement fault planes (dashed rectangles), nine vertically dipping fault planes that allow for opening and contracting displacement (representing rift zone and interwoven fault zone displacements (solid lines, model fault traces)). Along the Upper East Rift, strike-slip motion is also permitted. Four magmatic sources, which can inflate and deflate to accommodate the influx or drainage of magma, are marked as circles. The five model features that comprise our base model when testing source combinations (see Section 3.2 for details) are denoted in black and include the Kīlauea décollement, Kīlauea summit, East Rift, Upper East Rift, and Southwest Rift-1. An animation showing the 15 possible model features at depth with geometry parameter values from Table 1 can be found in our supporting data files.

impacted, a given model source are also noted in Figure 6. Four magmatic sources, which can inflate and/or deflate to accommodate the influx or drainage of magma, were included, representing the summits of Kīlauea and Mauna Loa, Mauna Ulu located in the Upper East Rift (which was active at least from 1969 to 1976 based on surface observations (Byrnes et al., 2004; Swanson, 1973)), and Pu'u 'Ō'ō located in the East Rift, where surface activity was first observed in 1983 (Gillard, Wyss, & Okubo, 1996) and persisted for 35+ years (Garcia et al., 2021). The remaining 11 model sources represent fault planes. Two faults are configured to represent Kīlauea and Mauna Loa low-angle décollements and were constrained to allow for thrusting, updip (southeastward) motion only. Nine other sources were constructed as vertical planes to represent rift zones and their interwoven fault zone systems. They accommodate dilation and contraction normal to the vertical faults (e.g., Owen, Segall, Lisowski, Miklius, Murray, et al., 2000; Swanson et al., 1976). The Upper East Rift, just south of Kīlauea's summit, also allowed for strike-slip displacement, similar to the Owen, Segall, Lisowski, Miklius, Murray, et al. (2000) solution. We note that, although it is clearly an important structural feature for the long-term evolution of the south flank, and had measured displacements during the 1975 earthquake, we found that including an element to represent the Hilina fault system did not influence our model results, so we chose not to include it.

All fault planes were divided into 2 × 2 km patches to allow the model to resolve varying magnitude and location of slip/opening along the planes. The patched faults thus allow us to search a larger region where potential displacement could occur without requiring homogeneous slip on each fault plane. This adds an additional

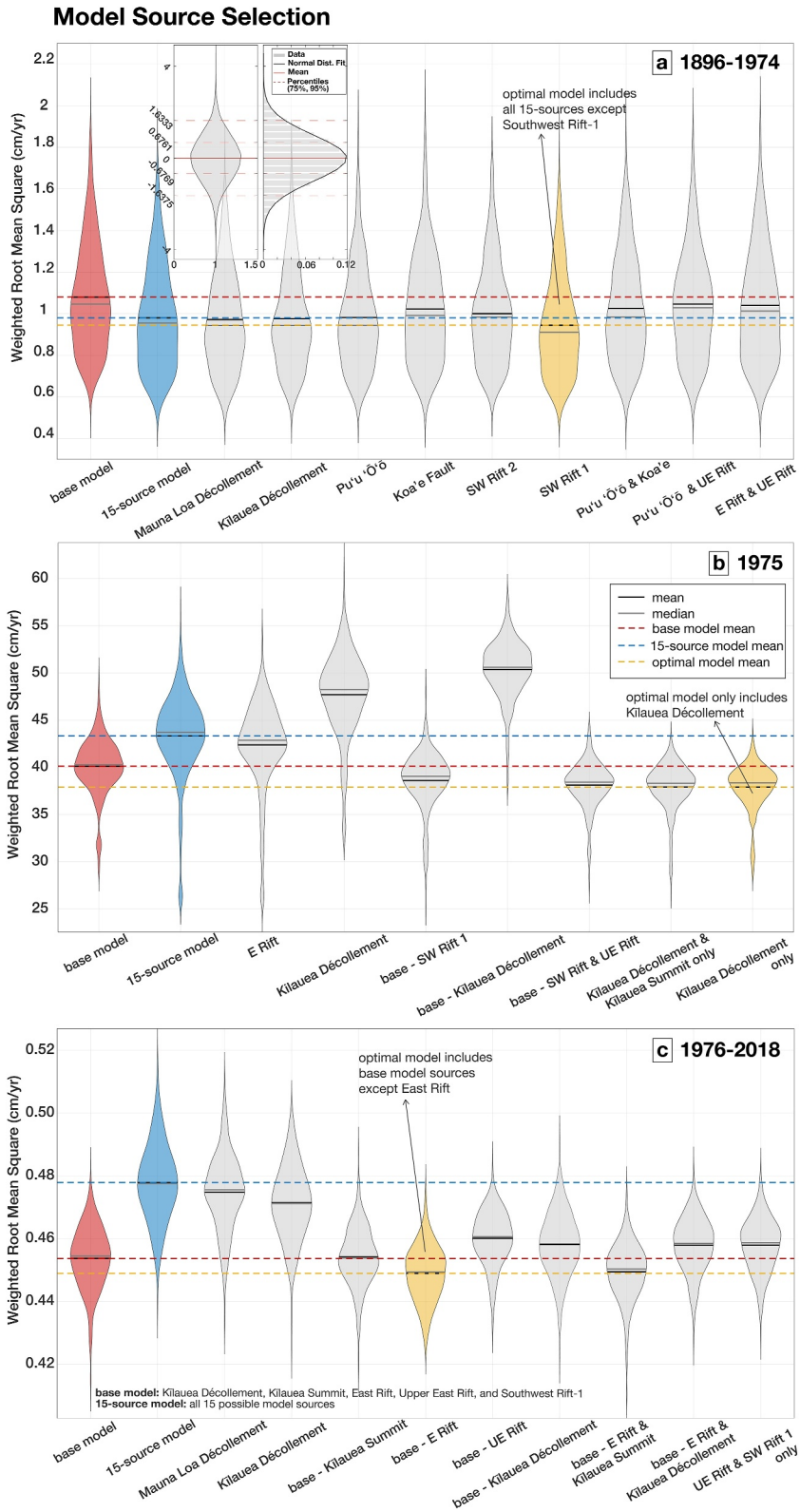

Figure 7.

component of complexity to the model but allows for more realistic patterns of slip to be resolved based on the displacement observations (e.g., Got et al., 1994; Owen, Segall, Lisowski, Miklius, Murray, et al., 2000).

Our initial analytical model was constructed using geometry parameters (i.e., strike, dip, depth) based on a priori values determined by previous studies for each model source. We then estimated slip and volume changes for the various sources and periods (before, during, and after the 1975 Kalapana earthquake) using cross-validation techniques. Finally, we revisited the geometry parameters, adjusting their values to minimize prediction error while holding slip and volume changes constant.

The a priori value for the centroid depth for Kīlauea's décollement was 10 km (e.g., Cannon et al., 2001; Crosson & Endo, 1981; Got & Okubo, 2003; Lipman et al., 1985; Morgan et al., 2000; Phillips et al., 2008; Swanson et al., 1976); the décollement was also assigned an a-priori low-angle northwest dip of 10° (e.g., Cervelli et al., 2002; Ma et al., 1999), a strike of 62° east of north, or parallel to the East Rift (Montgomery-Brown et al., 2011; Owen, Segall, Lisowski, Miklius, Murray, et al., 2000), and was positioned/emplaced to encompass both the on- and off-shore regions south of Kīlauea's summit that extend past both the Southwest and East Rift Zones (e.g., Delaney et al., 1998; Denlinger & Okubo, 1995). As our older data sets have limited accuracy, we assume that the decollement is sufficiently well described by a single plane despite evidence of some deepening to the southwest due to curvature caused by the island load. This might result in a small relative underestimate of the slip for the western portion of the decollement with respect to the eastern portion, and a consequent slight angular rotation error of modeled surface motion vectors. Mauna Loa's décollement was assigned an initial centroid depth of 12 km, a shallow, northwest dip of 5°, and a strike of ∼45° east of north (Walter & Amelung, 2006). It was emplaced to meet the northwest edge of Kīlauea's décollement (Lockwood et al., 1999), where the 2 décollements also slightly overlap. The other model faults and rift zone planes were vertical (Owen, Segall, Lisowski, Miklius, Murray, et al., 2000; Swanson et al., 1976) from the surface to a maximum depth of 10 km, and were not permitted to intersect the Kīlauea or Mauna Loa décollements. Faults and rift zone planes were allowed this large range in depth to accommodate potential shallow (3–5 km, Gillard, Rubin, & Okubo, 1996) and deep down to 12 km depth (Owen, Segall, Lisowski, Miklius, Murray, et al., 2000) displacements that mainly result from shallow magmatic intrusions and deep magmatic pressure causing slip along weaker layers of the crust that facilitates gravitational collapse. This 0–10 km depth range is similar to previous studies, and allows our model to explore a larger area to resolve the location of slip at depth needed to match observations.

The strikes and lengths of the faults and rift zones were determined based on mapped surface traces. The positions of the four magmatic sources were based on locations reported by the U.S. Geodetic Survey (www.usgs.gov). The depth of Kīlauea's magma chamber was constrained to be less than 6 km below the surface (Wright & Klein, 2014), while Mauna Loa's magma chamber was constrained to be ∼5 km (Amelung et al., 2007). Mauna Ulu and Pu‘u ‘Ō‘ō were constrained to a less than 3 km depth as these magmatic sources are widely associated with shallow rift zone eruptions (e.g., Delaney et al., 1998; Garcia et al., 2021). We assume a Poisson's ratio of 0.25 within our model.

3.2. Model Optimization

3.2.1. Defining Optimal Model Source Combinations Throughout Time

Given the large number of possible sources, the complexity of the region, and the potential interaction of these sources, one of our goals was to find the optimal combination of sources for each time period able to reproduce the

Figure 7. The weighted root-mean square (WRMS) distribution displayed as violin plots for all 5-fold cross-validation iterations for a subset of the considered model source combinations for time periods (a) 1896–1974, (b) 1975, and (c) 1976–2018. The labels along the *x*-axis indicate the combination of model sources. The "base" model includes the Kīlauea décollement, Kīlauea summit, East Rift, Upper East Rift, and Southwest Rift-1 (sources denoted in black inthis figure). The 15-source model indicates that all 15 of the possible model sources were used within the model. A label with a single source, such as "Pu‘u ‘Ō‘ō" in (a) refers to the 15-source model with the labeled source removed. For example, "Pu‘u ‘Ō‘ō" means that all of the 15 possible model sources were utilized except for the Pu‘u ‘Ō‘ō source. Alternatively, when a label refers to "base," like "base-Kīlauea Summit" (in c), this means that all of the sources within the base model were used except Kīlauea Summit. Lastly, when "only" is used at the end of a label, such as "Kīlauea Décollement only" (in b), then only the listed source(s) were used. The optimal source combination distribution (having the lowest average WRMS prediction error for each time period) is shown in yellow. The distribution for the base model is shown in red. The distribution for the 15-source model is shown in blue. The optimal model for 1896–1974 is the 15-source model with Southwest Rift-1 removed; the optimal model for 1975 includes only the Kīlauea Décollement and the optimal model for 1976–2018 is the base model with the East Rift removed. The inset in panel (a) shows a violin plot for a normal distribution with the mean, 75th and 90th percentiles marked. Wider sections of the violin plots represent higher probabilities.

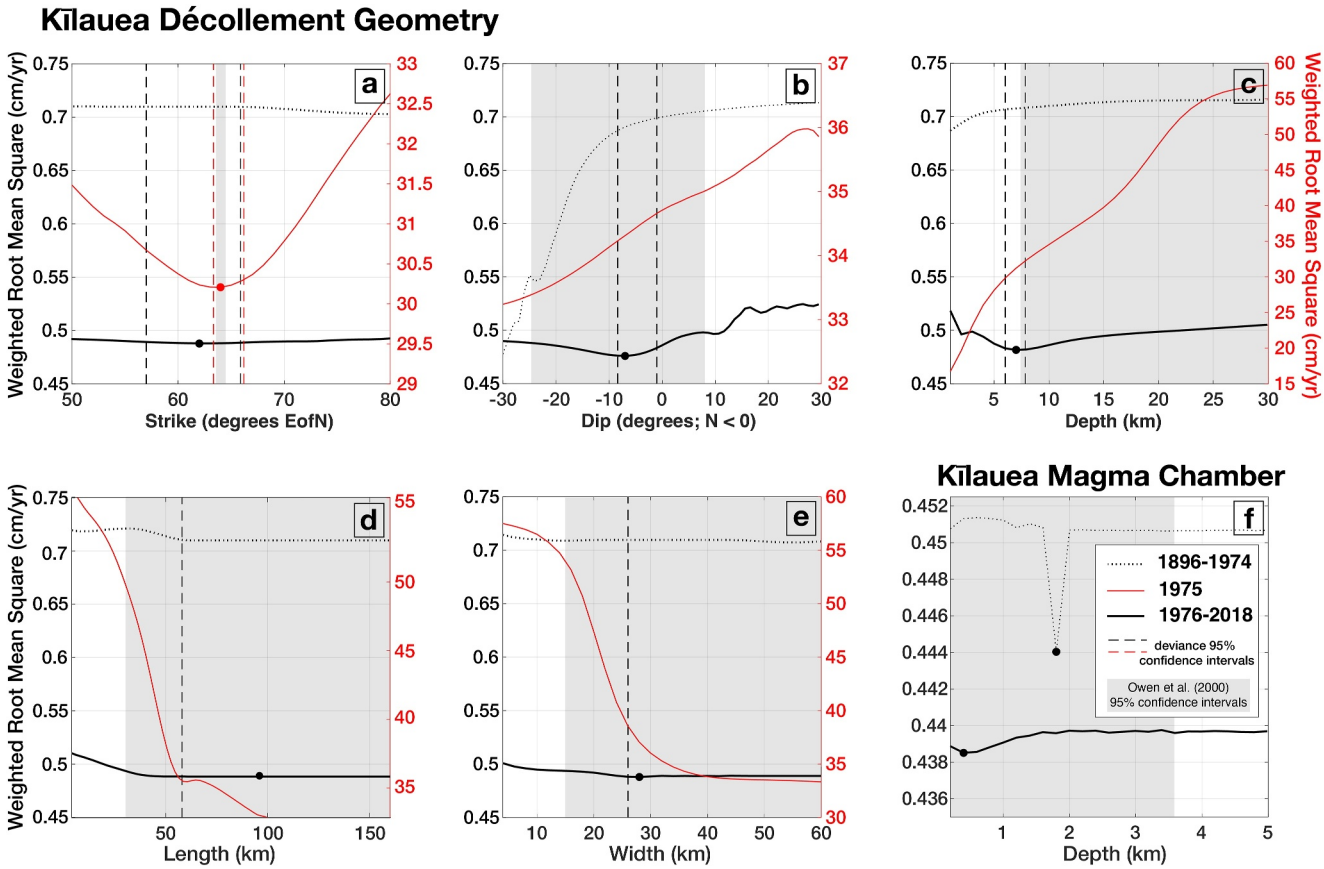

Figure 8. The weighted root-mean square (WRMS) prediction error for Kilauea's decollement geometry (a–e) and magma chamber depth (f). The 1896–1974 WRMS results are shown as black dotted lines. The 1975 Kalapana earthquake time period results are shown as red solid lines. The 1976–2018 WRMS results are shown as black solid lines. The strike, dip, and depth (structure) parameters specifically resolve model source characteristics, while the length and width parameters provide guidance for our model construction. When a minimum WRMS was found for a given parameter, 95% confidence intervals (dashed black vertical lines for before and after 1975 time period solutions; dashed red vertical lines for 1975 solutions) were determined by the deviance from the best fit value. A lower bound for the confidence intervals was resolved only for the length and width geometry parameters. An analogous geometry parameter search was conducted for each model source and each time period, as detailed in Figure S1 in Supporting Information S1. The 95% confidence intervals from the analysis of Owen, Segall, Lisowski, Miklius, Murray, et al. (2000) are also shown for comparison. The optimal geometry parameter values identified for each model source are provided in Table 1.

observations without overfitting the data. If all of the data were utilized for inversion, overfitting would be likely, especially when there are numerous model sources as the prediction error will nearly always decrease as the number of sources increases. To avoid this, we utilized a 5-fold cross-validation technique (e.g., James et al., 2013).

Within each time period source geometry parameters (such as dip, depth, etc.) were fixed at the a priori values mentioned above. Then the observations were randomized and 1/5 of the observations (the validation set) were set aside to be later used for model validation, while the remaining 4/5's of the data (training set) were used to build the model of slip and volume changes. In extracting the validation set, we required that the original ratio of the number of observations per data set type remain the same. For example, if EDM observations were 50% of all the observations for a specific time period, then the training set would also be 50% EDM observations.

To estimate the rate parameters (patched slip rates or volume changes) at each model source we used the source Green's functions and a weighted linear least squares solution (Equation 1). The weighting matrix used in the inversion was based on the uncertainties of the observations such that observations with low uncertainties had a higher weight and more influence on the solution. Equation 1 shows an example inversion set-up with all five geodetic data types: triangulation, EDM, leveling, GNSS, and PS data.

$$\sqrt{\left[\begin{pmatrix} \frac{1}{\overline{e}_{\text{tri}}} & 0 & \cdots & \cdots & 0 \\ 0 & \frac{1}{\overline{e}_r} & \vdots & \vdots & \vdots \\ \vdots & \vdots & \frac{1}{\overline{e}_h} & \vdots & \vdots \\ \vdots & \vdots & \vdots & \frac{1}{\overline{e}_{\text{GNSS}}} & 0 \\ 0 & \cdots & \cdots & 0 & \frac{1}{\overline{e}_V} \end{pmatrix}\right]}\left(\begin{bmatrix} \overline{G}_{\text{tri}} \\ \overline{G}_{\text{EDM}} \\ \overline{G}_{\text{level}} \\ \overline{G}_{\text{GNSS}} \\ \overline{G}_{\text{PS}} \end{bmatrix}\begin{bmatrix} \overline{m}_1 \\ \vdots \\ \overline{m}_N \end{bmatrix} = \begin{bmatrix} \overline{v}_{\text{tri}} \\ \overline{r} \\ \overline{h} \\ \overline{v}_{\text{GNSS}} \\ \overline{V} \end{bmatrix}\right) \quad (1)$$

The first matrix represents the weighting scheme derived from the square root of the inverse data covariance matrix ($\underline{e}$). The second matrix contains the Green's functions for modeled displacements (G) determined from the analytical dislocation model (Mogi, 1958; Okada, 1985) described in Section 3.1, where the subscripts relate to the five different types of data sets and their observation locations. We solve for the rate parameters (either the patched slip rates or volume changes) for each model source, $\underline{m}_{1:N}$, that minimize the prediction error for the training set. The training set data consists of: $\underline{v}_{\text{tri}}$ is the 1896–1970 triangulation horizontal velocity measurements, $\underline{r}$ is the range displacement rate observations from the 1970–1990 EDM data set, $\underline{h}$ is the height displacement rate observations from the 1963–2012 leveling data set, $\underline{v}_{\text{GNSS}}$ contains both the 1990–1996 and 1996–2018 GNSS horizontal velocity measurements, and $\underline{V}$ is the vertical displacement rate observations from the 2000–2004 offshore PS data set.

We then tested the accuracy of the model solution (o_p) by predicting the validation set observations (o), obtaining a weighted root-mean square prediction error (WRMS, Equation 2).

$$\text{WRMS} = \sqrt{\frac{\sum_{i=1}^{n}\left(\frac{o(i)-o_p(i)}{e(i)}\right)^2}{\sum_{i=1}^{n}\frac{1}{e(i)^2}}} \quad (2)$$

The cross-validation procedure (randomizing the data, separating it into training and validation sets, inverting the training set of data to obtain a model solution, and calculating the prediction error on the validation set) was repeated a minimum of 500 times for each model source combination considered. For each of our three time periods the optimal source combination was taken to be the combination with the lowest WRMS averaged over the 500 runs. The WRMS results for a subset of the source combinations are displayed as violin plots in Figure 7. Wider sections of the violin plot indicate a higher probability of the source combination.

To determine which combinations of model sources to consider, we first tested a five-source base model and 15-source full model for each time period. The base model consisted of the Kīlauea décollement, Kīlauea summit, East Rift, Upper East Rift, and Southwest Rift-1, and was constructed to be similar to the final model solutions of Owen, Segall, Lisowski, Miklius, Murray, et al. (2000). The 15-source model consisted of all 15 possible sources considered in this study. After determining which of these two models resulted in a lower average WRMS, we employed backward stepwise selection by removing single model sources from that model (James et al., 2013). This allowed us to efficiently search for the optimal combination of model features for each time period.

When considering observations from 1896 to 1974 (Figure 7a), the 15-source model had a lower average WRMS than the base model. We tried removing sources such as the Koa'e Fault, Southwest Rift-2, and combinations of Pu‘u ‘Ō‘ō, the Koa'e Fault, and the East and Upper East Rifts, but that increased the average WRMS. The only source that significantly lowered the WRMS when removed, was the Southwest Rift-1. Our optimal model for the 1896–1974 time period therefore consists of all 15 sources except the Southwest Rift-1. This pre-earthquake period of 1896–1974 also had a higher WRMS range than the post-earthquake time period due to decreased data volume and resolution for these early observations.

The 1975 time period (Figure 7b), encompassing the M_w7.7 Kalapana earthquake, had a lower prediction error for the base model than for the 15-source model. We also found that removing the Kīlauea Décollement from either the base or 15-source model caused a significant increase in average WRMS, highlighting the necessity of that source throughout this active time period. We ultimately determined that the lowest average WRMS resulted from using the Kīlauea Décollement as the only deformation source. This simple interpretation of deformation sources is reasonable, despite the short (<1 year) time period, because the 1975 earthquake dominated the motions. The magnitudes of displacement observations, with an average total slip of 7.9 m along the décollement plane (Nettles & Ekström, 2004), were much larger than displacements related to other sources seen within the alternative time periods.

Similar to the 1975 observations, the 1976–2018 time period (Figure 7c) also required a much simpler combination of model sources than the time period preceding the 1975 earthquake: the Kīlauea Décollement and Summit, the Upper East Rift, and the Southwest Rift-1. This post-1975 time period had the largest number of observations, as well as the lowest observation uncertainties, resulting in improved model resolution. The Upper East Rift and Kīlauea Décollement were also important for reproducing the observed displacements following the 1975 earthquake, as WRMS values significantly increased when those model sources were removed.

3.2.2. Refining Model Structural Parameters

To further refine our optimal source-combo models, we explored the geometry parameters, such as strike, dip, and depth for each fault plane source, and source depth for each magma chamber (Figure 9). If a minimum WRMS was found for a geometry parameter, we attempted to find the 95% confidence interval for the solution based on the deviance from the geometry parameter value that minimized the WRMS. To do this, we first calculated the prediction error (WSQ, Equation 3) over a range of values using the observations (o) model predictions (o_p) and the process error (E_p) (Equation 4).

$$\mathrm{WSQ} = \sum_{i=1}^{n} (o(i) - o_p(i))^2 / E_p(i)^2 \tag{3}$$

E_p is unique for each type of data set and is determined by the total number of observations in the data set (N_d) and the misfit between corresponding observations (o_d) and model estimates (o_{pd}).

$$E_p = \sqrt{(1/N_d) \sum_{i=1}^{N_d} (o_d(i) - o_{pd}(i))^2} \tag{4}$$

The WSQ uses process error instead of observation errors because the observations are highly correlated within each data set type, especially the EDM and leveling data sets that have observations based on geometric network solutions. The process errors are inherently larger than observational errors because the modeling process that generates each solution has uncertainties comparable in size to those of the data.

Lastly, we estimated confidence intervals based on the deviance of the WSQ solutions. The deviance function, $D(\theta)$, is defined as the difference between the two log-likelihoods, which can be reduced to the difference between two WSQ (Coles, 2001). We obtain the deviance for each parameter value θ by subtracting the $\mathrm{WSQ}(\theta_o)$, the minimum WSQ, from $\mathrm{WSQ}(\theta)$ (Equation 5).

$$D(\theta) = \mathrm{WSQ}(\theta) - \mathrm{WSQ}(\theta_o). \tag{5}$$

As we are varying only one geometry parameter at a time, we can again follow Coles (2001) and note that the relevant Chi-Squared (χ^2) distribution that relates to the deviance function has just one degree of freedom. We can thus approximate the $(1 - \alpha)$ confidence region (C_α) for θ_o based on the quantiles of the χ^2 distribution, c_α (Equation 6). We determine the 95% confidence interval ($\alpha = 0.05$) with one degree of freedom, so that $c_\alpha = 3.84$ and all $D(\theta)$ less than or equal to c_α fall within our confidence region.

$$C_\alpha = \{\theta : D(\theta) \leq c_\alpha\} \tag{6}$$

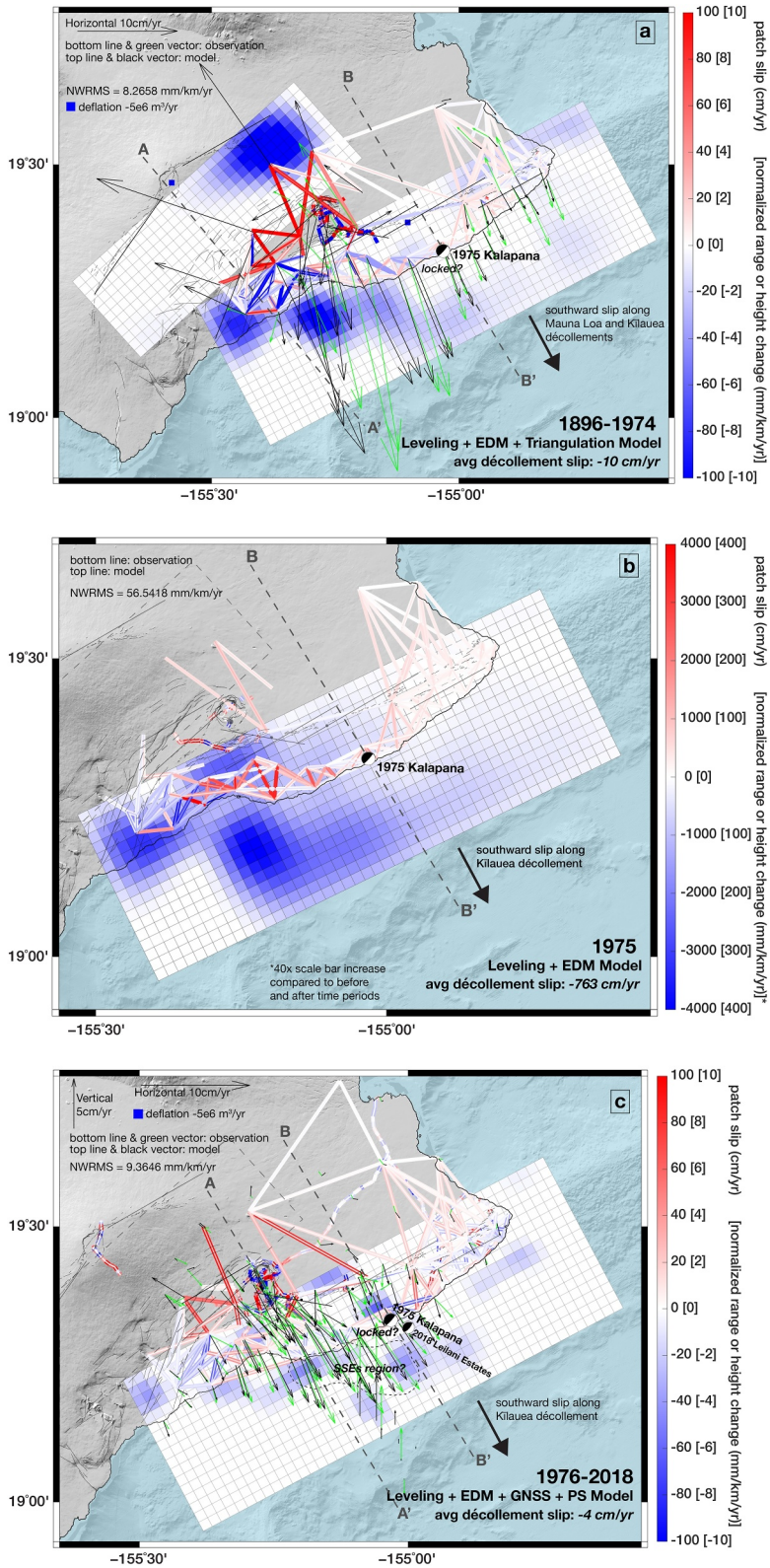

Figure 9.

The results of this geometry parameter analysis are provided in Figure 8; when a minimum WRMS was found for a given geometry parameter, 95% confidence intervals are marked as dashed vertical lines. This method of refining geometry parameters was particularly successful for the 1976–2018 time period following the 1975 Kalapana earthquake, the period with the largest number of observations and lowest uncertainty. We additionally compared our deviance-derived 95% confidence intervals to the 95% confidence levels reported in Owen, Segall, Lisowski, Miklius, Murray, et al. (2000) (gray regions in Figure 8). All of our a priori values and tested geometry parameter ranges fall within those used throughout Owen, Segall, Lisowski, Miklius, Murray, et al. (2000). We note that the preferred depth for the decollement is shallower than the depth found for seismic solutions for the 1975 earthquake that is assumed to have occurred on it. This is consistent with other geodetic studies that have found (Montgomery-Brown et al., 2009) that the relatively simple models used for standard geodetic inversions generate shallow preferred depth solutions. More complex models incorporating layered rheologies and fully-correcting for topography generate depths that match seismic solutions. However, this requires additional parameters and would greatly complicate the analysis and interpretation and so were not included here.

Geometry parameters that minimized WRMS, as reported in Table 1, were used for the remainder of this study. While the strike, dip, and depth parameters specifically resolve model source geometric characteristics based on the observed surface displacements, the length and width parameters provide only guidance for our model construction. The patched slip solutions allow realistic slip patterns to form on the fault plane. Geometry parameters for which a minimum WRMS could not be found are unconstrained by the observations, so initial a priori values were retained in the final models. Additionally, we note that sometimes a minimum WRMS is found, but the WRMS range is very small (like the parameter search for the depth of Kīlauea's magma chamber in Figure 8f). This suggests that again the model is not well enough constrained by the observations to find a robust minimum value and that there is a large range of values that perform well. Ensemble results for all geometry parameters (including the remaining model sources not illustrated in Figure 8) can be found in Figure S1 in Supporting Information S1.

4. Results

The different data sets provide different levels of constraints on our model parameters, depending both on the spatial distribution of the observation locations and the type and accuracy of the observations themselves. Results from models inverted using each data set individually are presented in Supporting Information S1 and show that they each capture the same primary features of the deformation field for each time period. Forward models were run for each time period's optimal source configuration with refined geometry parameter values (see Table 1) to predict the displacement from each type of geodetic data (Figure S2 in Supporting Information S1). Forward modeling results for combined displacements from all available data sets are provided in Figure 9 (map view) and 10 (depth view). Average slip rates and volume change (rate parameters) for each active model source resulting from the combined data sets for each time period can be found in Table 2. Seismicity locations and depths throughout the time period 1933–2018 (Figure 11) were also considered when analyzing these results, as well as modeled displacement time series for a few key observation locations that were occupied during multiple campaigns, all of which are discussed in detail in the remainder of this section.

Figure 9. Map view patched fault slip rates and magma chamber volume change rates based on combined data sets. (a) Solutions from the combined triangulation, EDM and leveling data sets available for the 1896–1974 time period, prior to the 1975 Kalapana earthquake. (b) Solutions from the combined EDM and leveling data sets available for the 1975 time period, encompassing the M_w7.7 Kalapana earthquake. (c) Solutions from the combined EDM, leveling, Global Navigation Satellite System (GNSS), and pressure sensor (PS) data sets available for the 1976–2018 time period, following the 1975 Kalapana earthquake. Slip/opening rate in cm/yr is shown along all active sources for each time period. The Kīlauea and Mauna Loa décollement slip results can be readily seen in this map view orientation, where negative (blue) slip depicts southward motion. The slip along the additional vertical fault planes and magma chamber volume change and depth locations can be seen in Figure 11 and within the animations provided as supporting files for each time period. An example magma chamber with a deflation rate of $-5E+6$ m^3/yr is also shown in the upper left corner for time periods that require magmatic sources. Also, note the change in scale for the color bar during the 1975 time period compared to the before and after time periods. Observed displacements are shown as green vectors for trilateration, GNSS, and PS observations and as the thicker, bottom line for EDM and leveling observations. Modeled trilateration, GNSS, and PS displacements are shown as black vectors, while modeled EDM and leveling displacements are shown as the narrower, top lines. The average slip/opening along the fault planes and average volume change for magmatic sources active within each of the three time periods is reported in Table 2. The weighted root-mean square prediction error, normalized by the length of the baseline of each observation (NWRMS), is displayed for each time period as strain rates (mm/km/yr). The length of the baseline for single station observation data, such as GNSS, is assumed to be 1 km. The region where slow slip events may occur is outlined with black dashes in (c) and is adopted from Foster et al. (2013). A-A′ and B-B′ indicate profiles in key regions for each time period where we analyze the resulting stress at depth in Figure 12, and Figures S3–S5 in Supporting Information S1.

Table 1
Geometry Parameter Values Utilized in the Optimal Models; A Priori Values That Differ From the Optimal Values Are Shown in Parentheses

1896–1974	Strike (EofN)	Dip ($N < 0°$)	Length (km)	Width (km)	Depth (km)	Longitude	Latitude
Kīlauea Décollement	62°	−7° (−10°)	83	30	7.0 (10.0)	−155.065°	19.288°
Mauna Loa Décollement	48°	−5°	48	16	11.0 (12.0)	−155.495°	19.387°
Lower East Rift	61°	90°	16	6	3.0	−154.896°	19.450°
East Rift	60°	90°	26	8	4.0	−155.052°	19.416°
Upper East Rift	100°	90°	16	8	4.0	−155.216°	19.367°
Southwest Rift-2	21°	90°	22	8	4.0	−155.459°	19.247°
Northeast Rift	60°	90°	22	10	5.0	−155.478°	19.540°
Northwest Rift	215°	90°	26	10	5.0	−155.674°	19.334°
Mauna Ulu Dike	60°	90°	24	6	3.0	−155.182°	19.367°
Koa'e Fault	48°	90°	20	8	4.0	−155.355°	19.350°
Kīlauea Magma Chamber	–	–	–	–	1.8 (<6.0)	−155.273°	19.391°
Mauna Loa Magma Chamber	–	–	–	–	1.2 (5.0)	−155.589°	19.457°
Mauna Ulu Magma Chamber	–	–	–	–	0.8 (<3.0)	−155.201°	19.367°
Pu‘u ‘Ō‘ō Magma Chamber	–	–	–	–	0.4 (<3.0)	−155.105°	19.386°
1975	Strike (EofN)	Dip ($N < 0°$)	Length (km)	Width (km)	Depth (km)	Longitude	Latitude
Kīlauea Décollement	64° (62°)	−7° (−10°)	83	30	7.0 (10.0)	−155.065°	19.288°
1976–2018	Strike (EofN)	Dip ($N < 0°$)	Length (km)	Width (km)	Depth (km)	Longitude	Latitude
Kīlauea Décollement	62°	−7° (−10°)	83	30	7.0 (10.0)	−155.065°	19.288°
Upper East Rift	100°	90°	16	8	4.0	−155.216°	19.367°
Southwest Rift-1	60°	90°	16	8	4.0	−155.361°	19.393°
Kīlauea Magma Chamber	–	–	–	–	0.4 (<6.0)	−155.273°	19.391°

Note. Three time periods surrounding the 1975 Kalapana earthquake were analyzed: 1896–1974, 1975, and 1976–2018. Strike is shown in relative degrees east of north (north = 0°), a negative dip indicates a northward dipping plane, a length and width for each patched fault plane is provided, and the depth, longitude, and latitude refer to the centroid locations of either a fault plane or magmatic source. Vertical fault planes (dip = 90°) extend from the surface (0 km) to 2x their centroid depth. For example, the East Rift plane has a centroid depth of 4 km and a width of 8 km in the vertical direction, meaning its depth ranges from 0 to 8 km below the surface.

4.1. 1896–1974 Deformation Model

The 1896–1974 time period (Figures 10a and 11a; Average slip along the fault planes and average volume change for magmatic sources is reported in Table 2) results based on the combined triangulation, EDM, and leveling data sets show high magnitude slip occurring west of the 1975 epicenter and minimal to no slip occurring near the earthquake's epicenter along the Kīlauea décollement. This suggests that the portion of the décollement plane from which slip nucleated during this large magnitude earthquake may have been locked prior to rupture. The average slip estimated across the entire Kīlauea fault plane from the ensemble of data is 10 cm/yr of southward displacement (Figure 10a). The magnitude of slip drops toward the seaward edge of the décollement. Although the available data have limited ability to resolve offshore slip, this is consistent with the outer bench acting as a buttress (Morgan et al., 2003), acting as a boundary to seaward slip, and stabilizing the south flank structure. There is also high-magnitude slip found on the eastern end of the Mauna Loa décollement, north of Kīlauea's summit. Our model also results in significant northwestward vectors for some of the Mauna Loa sites at the very edge of our observing network. We hypothesize that this is representative of the difficulties in jointly analyzing data sets spanning such a large time window, combined with poor geometric distribution of observations for model sources at the very edge of our study region, and that these vectors, the high-magnitude slip patch on Mauna Loa's décollement, and the long-term contraction of Mauna Loa's rift-zones may not be robust results.

There are 12 other model sources active in this “before” time period (Figure 10a). Eight of these are fault planes and four are magmatic sources. Both the Northeast and Northwest Rifts along Mauna Loa, and the Southwest Rift-2, East, and Lower East Rifts within Kīlauea's edifice, resolve average contracting displacement leading up to the

Table 2
Rate Parameters (Average Slip/Opening Rate (cm/yr)), As Well As Cumulative Slip Over the Time Period (cm), and Volume Change (10^6 m^3/yr) for Each Source During the Three Time Periods of This Study

$\underline{s}$ = average slip rate (cm/yr) s = cumulative slip (cm) δV = volume change (10^6 m^3/yr)	1896–1974	1975	1976–2018
Kīlauea Décollement $\underline{s}$ (s)	−10.14 (−790.92)	−763.38 (−763.38)	−3.68 (−154.56)
Mauna Loa Décollement $\underline{s}$ (s)	−14.83 (−1156.74)	–	–
Lower East Rift $\underline{s}$ (s)	−3.01 (−234.78)	–	–
East Rift $\underline{s}$ (s)	−0.17 (−13.26)	–	–
Upper East Rift $\underline{s}$ (s) [open]	10.17 (793.26)	–	13.10 (550.20)
Upper East Rift $\underline{s}$ (s) [strike]	9.14 (712.92)	–	−3.85 (−161.70)
Southwest Rift-1 $\underline{s}$ (s)	–	–	2.05 (86.10)
Southwest Rift-2 $\underline{s}$ (s)	−0.75 (−58.5)	–	–
Northeast Rift $\underline{s}$ (s)	−44.54 (−3474.12)	–	–
Northwest Rift $\underline{s}$ (s)	−89.29 (−6964.62)	–	–
Mauna Ulu Dike $\underline{s}$ (s)	2.62 (204.36)	–	–
Koa'e Fault $\underline{s}$ (s)	48.29 (3766.62)	–	–
Kīlauea Magma Chamber δV	4.54 (354.12)	–	−6.55 (−275.10)
Mauna Loa Magma Chamber δV	−3.70 (−295.62)	–	–
Mauna Ulu Magma Chamber δV	−5.62 (−438.36)	–	–
Pu‘u ‘Ō‘ō Magma Chamber δV	−3.74 (−291.72)	–	–

Note. Model results are based on the combined inversion of all available data within each time period (Figures 9 and 10). The low-angle décollement planes were only allowed thrusting displacement, where negative slip represents updip or southward motion. All other fault planes were vertical and allowed opening or closing displacements, where positive values represent opening motion, and negative represents closing motion. We note that contracting rifts might not normally be expected but are necessary to optimally fit the data observations. Additionally, the Upper East Rift was also allowed strike-slip displacement, where positive slip corresponds to right-lateral motion and negative slip refers to left-lateral motion. A positive volume change denotes inflation at magmatic point sources, while negative volume change denotes deflation.

1975 Kalapana earthquake. The Koa'e Fault, Upper East Rift, and Mauna Ulu fault planes, however, all resolve average extension and are also located nearest to Kīlauea's summit and the area where the highest amount of extension from decollement slip. The Kīlauea magma chamber additionally shows inflation (4.54E + 6 m^3/yr), aligning with the observed seismicity and eruptive events that preceded the earthquake, such as the 1974 Southwest Rift/Koa'e eruptions (Lockwood et al., 1999). Conversely, the Mauna Loa, Mauna Ulu, and Pu‘u ‘Ō‘ō sources indicate various levels of deflation (−3.70, −5.62, and −3.74E + 6 m^3/yr, respectively) leading up to the 1975 earthquake. Even though surface eruptions do not begin near Pu‘u ‘Ō‘ō until a couple of years after 1975, our cross-validation approach still found it necessary to include a model source at Pu‘u ‘Ō‘ō for this time period, indicating a magma reservoir at or near this location caused deformation before the 1983 surface eruption.

Figure 11 plots modeled slip rates for some example locations. The high magnitude slip for the western portion of Kīlauea's décollement is reflected in this modeled deformation time series for the Hilina site (red station in Figures 11a and 11c). We see the least displacement leading up to 1975 at the Lower East Rift (Kaliu, yellow) and coastal (Kupapau, blue) stations. This coastal station is alongside the portion of the décollement that exhibits little slip during this period (Figure 9a), and coincides with the epicenter of the Kalapana earthquake. This is most likely a frictionally locked zone.

4.2. 1975 Deformation Model

The 1975 M_w7.7 Kalapana earthquake time period (Figure 9b) requires only the Kīlauea décollement to adequately model the EDM and leveling data and resolve southward slip across the majority of the Kīlauea décollement with an average rate of 763 cm/yr. Since this time period encompasses the full but brief earthquake event, which occurred within a single year, this rate is the same as the cumulative slip during the event. In contrast,

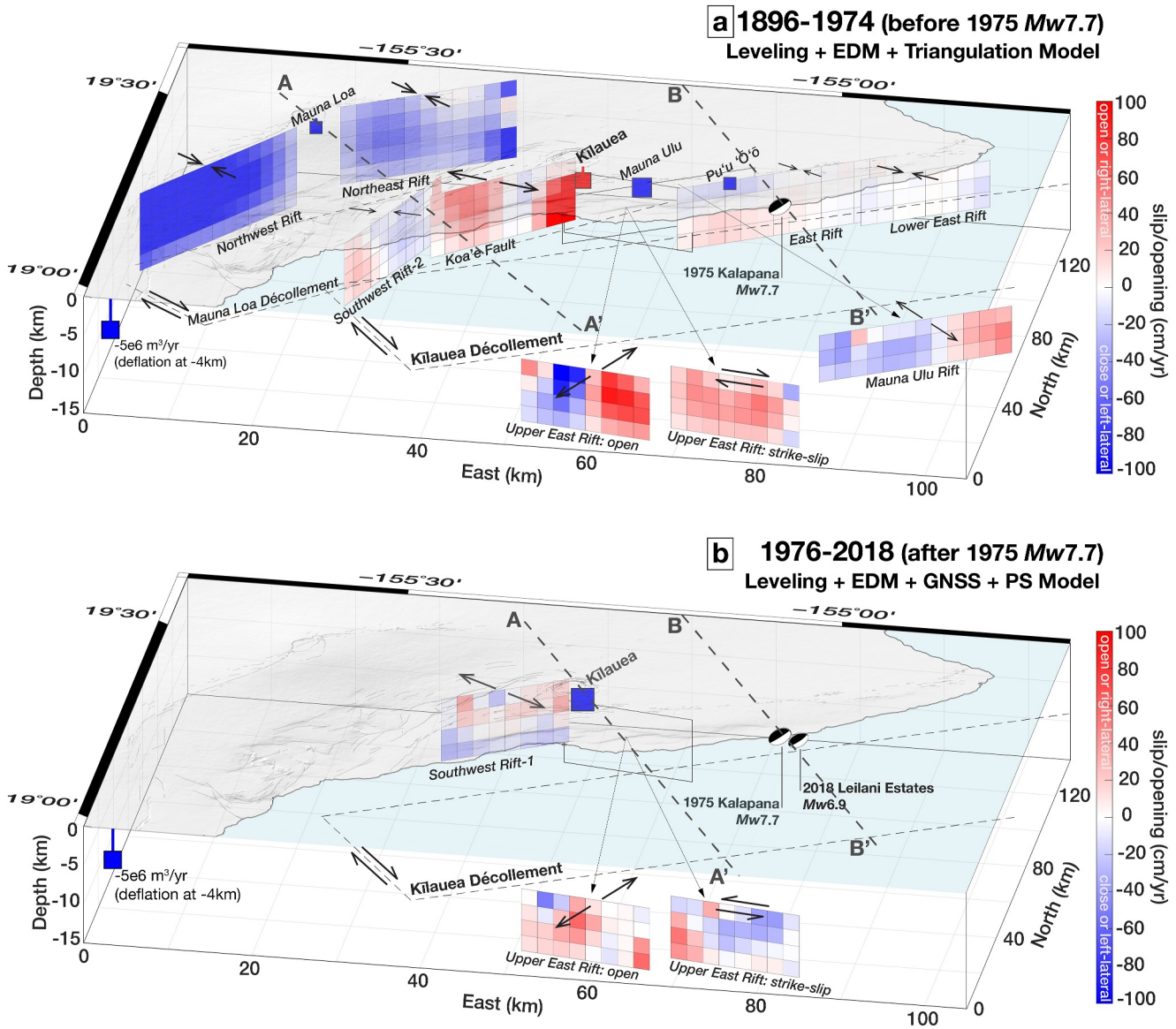

Figure 10. Model solutions of patched fault slip/opening rates and magma chamber volume change rates. (a) Slip/opening and volume change from combined triangulation, EDM and leveling data sets available for the 1896–1974 time period, prior to the 1975 Kalapana earthquake. (b) Slip/opening and volume change from the combined EDM, leveling, Global Navigation Satellite System, and pressure sensor data sets available for the 1976–2018 time period, following the 1975 Kalapana earthquake. The 1975 time period encompassing the M_w7.7 earthquake is omitted here as its only active model source was Kīlauea's décollement, which can be seen in Figure 9b. Slip/opening rate (cm/yr) is resolved along all active fault model sources for each time period, where large black arrows denote the mode and average direction of motion (all model source averages are specified in Table 2); negative (blue) depicts contraction or left-lateral strike-slip displacement and positive (red) depicts extension or right-lateral strike-slip displacement. Only the Upper East Rift is allowed strike-slip displacement. Scaled volume changes of magmatic point sources (squares plotted at depth, in m^3/yr; blue for deflation and red for inflation) are plotted as stem plots that connect from the surface to the depth of each magma chamber. An example magma chamber located 4 km below the surface and with a deflation rate of $-5E+6$ m^3/yr is shown in the lower left corner of both (a) and (b). Gray dashed rectangles denote the location of the active décollement(s) for each time period.

the time period prior to the earthquake spans decades, and the slip rate represents a true yearly average over that longer time frame. Again, we see the highest magnitude slip occurring beneath and just offshore of the Hilina fault system region, consistent with several previous studies showing large southward displacement here (e.g., Delaney et al., 1992; Lipman et al., 1985; Swanson et al., 1976). We note that the Hilina fault system was found to have slipped during the earthquake (Cannon et al., 2001; Lipman et al., 1985). As we do not have any source elements representing these faults, these observed displacements will therefore have to be accommodated as greater décollement slip for this region in our model. This may mean that the magnitude of slip for the portion seaward of

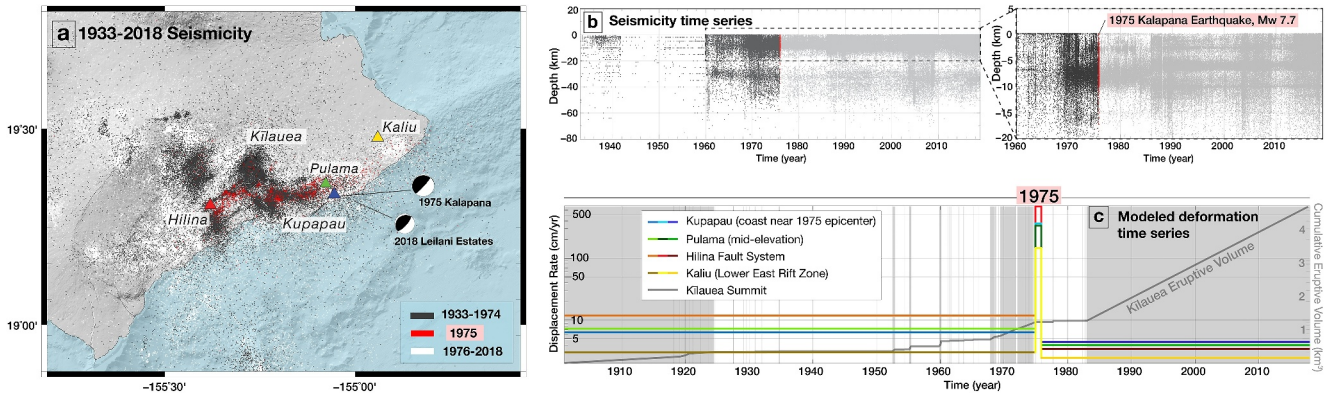

Figure 11. 1933–2018 seismicity and deformation throughout the Mauna Loa and Kīlauea regions. (a) Geographical locations of the earthquakes and key observation locations occupied by multiple data sets positioned at the coast, mid-elevation, in the Hilina fault system, and within the Lower East Rift Zone. (b) Seismicity time series showing the range of earthquake depths over time. Earthquakes that occurred before 1975 are shown in dark gray, during 1975 are red, and after 1975 are light gray or white. (c) Modeled deformation time series based on combined data sets (Figures 9 and 10) for four key stations whose locations are marked in (a). These deformation rates are also compared to the 1896–2018 cumulative eruptive volume of magma from Kīlauea (gray lines). Time series for the coastal station Kupapau (near the 1975 earthquake epicenter) is shown in shades of blue to represent before, during, and after 1975 displacement rates. The mid-elevation station Pulama is shown in green, the Hilina station within the Hilina fault system in red, and the Lower East Rift station, Kaliu, in yellow.

this system, alongside the Papa'u seamount, is higher than it should be. The consistency in the slip patch locations with the "before" period however, suggests that high slip rates did indeed occur here. For the 1975 period, high slip is predicted out to the seaward edge of the décollement. The geometry of our data sets only very weakly constrains slip here, but the solution suggests that slip may have extended further seaward than in the other periods. If this is the case, it would likely involve slip either along the thrust fault overlapping onto the outer bench (Morgan et al., 2003), or possibly on the décollement under the bench itself. If this latter were the case, the outer bench might represent less of a structural stabilizing effect than assumed.

4.3. 1976–2018 Deformation Model

The 1976–2018 time period following the 1975 Kalapana earthquake (Figures 9c and 10b) had the most data set types available for analysis, including EDM, leveling, GNSS and PS data. This time period had a particularly low weighted prediction error (i.e., WRMS normalized by the length of the baseline of each observation (NWRMS)) and also finds the lowest magnitude of average slip along Kīlauea's décollement of only 4 cm/yr of southward displacement (Figure 9c). This low average southward motion along the décollement is similar to previous studies' findings of ~6 cm/yr of southward displacement rates for Kīlauea's south flank (e.g., Delaney & Denlinger, 1999; Miklius et al., 2005). It is also lower than the average rate preceding the Kalapana earthquake of 10 cm/yr. Moreover, compared to the resolved slip pattern before the 1975 Kalapana earthquake, the slip is now distributed into smaller and more irregular patterns of deformation that encompasses both on- and off-shore areas of the Kīlauea décollement. This could indicate the spatial variability of mechanical properties and/or differences in effective stress that are thought to occur along the décollement (Lin et al., 2020). Overall, a much broader range of average slip rates (4–35 cm/yr of southward displacement) along Kīlauea's décollement was found for this time period of 1976–2018. This is likely at least partly due to the improved accuracy and spatial resolution of the data, but as all temporal variation over this period is modeled as a single static solution, temporal variation, and the superposition of multiple processes - for example, the SSEs first recognized during this time may contribute to the variation.

Along with the Kīlauea décollement, there are also three additional active model sources for the 1976–2018 time period: the Southwest Rift-1, Upper East Rift, and Kīlauea summit (Figure 11b). Unlike our results prior to the earthquake, Kīlauea's magma chamber after 1975 has a negative change in volume and deflates at a rate of $-6.55E+6$ m^3/yr. Deflation of this magnitude for Kīlauea was also found by Owen, Segall, Lisowski, Miklius, Murray, et al. (2000), who found a slightly lower deflation rate of up to $-2.00E+6$ m^3/yr for the 1990–1996 time period. This change from inflation at the summit prior to 1975 and deflation afterward was then followed by the first East Rift Zone eruptions in over a decade (1977 and 1983) and is consistent with the top-down inflation/deflation theory where changes at the summit can promote or inhibit magmatic intrusions into the surrounding rift zones (e.g., Baker & Amelung, 2015; Delaney & Denlinger, 1999). Additionally, both the Southwest Rift-1

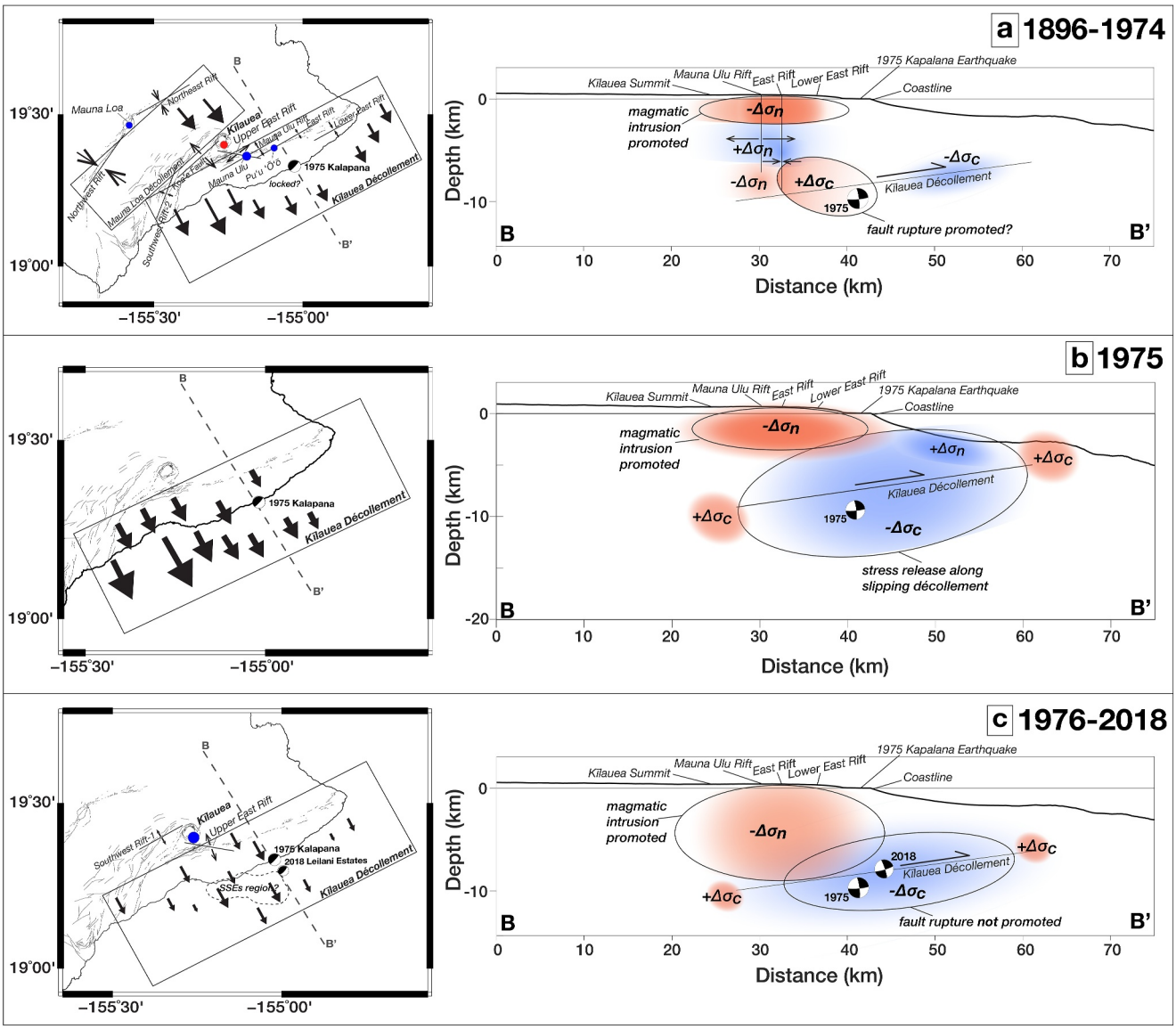

Figure 12. Simplified schematic of average slip direction and magnitude and magma chamber volume change solutions for each active source in map view (from Figures 9 and 10) and the resulting Coulomb stress changes ($\Delta\sigma_c$) based on a Kīlauea décollement receiver fault, and the normal stress changes ($\Delta\sigma_n$) based on the East Rift Zone receiver fault (from Figure S3 in Supporting Information S1). Black arrows denoting fault slip are scaled by magnitude. Net inflation of a magma chamber is shown as a red circle, net deflation is shown as a blue circle, and these are also scaled by magnitude. Coulomb stress changes that promote failure (positive) are highlighted in red, while Coulomb stress release changes (negative) are highlighted in blue. Normal stress changes that promote failure (negative) are highlighted in red, while normal stress release changes (positive) are highlighted in blue.

(4 cm/yr) and Upper East Rift (13 cm/yr) resolve extensional motion, indicating that the Upper East Rift has a greater displacement rate on average than the Kīlauea décollement for this time period. Furthermore, the displacement rates for all four example time series stations in Figure 12c are lower than their rates before 1975, with the largest displacement occurring along the coast at Kupapau station.

5. Discussion

The driving forces for stress accumulation along Kīlauea's décollement have been explained by a range of mechanisms, such as volcanic intrusions (e.g., Swanson et al., 1976), and gravitational instability arising from the increasing mass of the growing volcano (e.g., Delaney et al., 1998). These mechanisms produce an overall compressive stress environment, which drives the low-angle, thrusting décollements to transport material upslope

(southward in this case) over time. It is likely that it is a combination of these mechanisms that results in the secular southward slip along the décollement (e.g., Wright & Klein, 2014; Yin & Kelty, 2000).

The accumulation of stress along Kīlauea's décollement, and the resulting shortening of baselines across the subaerial flank, is probably strongly associated with the continuous seaward displacement of Kīlauea's south flank, which is frictionally resisted by coupling of the décollement (Liu et al., 2018). Day et al. (2005) note that repeated earthquakes like the 1975 Kalapana, and ~M_w8 1868 Great Ka'ū earthquake (Wyss, 1988) could cause extension and subsidence in the upper flank of Kilauea and compression and uplift of the toe region, accompanied by slump movement (i.e., Hilina normal faulting), which stabilizes Kīlauea and makes catastrophic failure of the volcano flank less likely.

5.1. Evolution of Slip Along Kīlauea's Décollement

It is clear from our model solutions that the magnitude and distribution of slip along Kīlauea's decollement has varied significantly through time. Prior to the 1975 M_w7.7 Kalapana earthquake, our results suggest that, while there was contraction beneath the Hilina fault system, there were large southward displacements, especially on the western edge of Kīlauea's decollement, which may be coupled with large southward displacements on the eastern edge of Mauna Loa's décollement. Spatial variability of slip on the décollement is consistent with the multiple types of seismic events observed in recent years with improved geodetic and geophysical observation techniques. Micro-seismicity, SSEs, and large magnitude ruptures like the Kalapana earthquake all occur along the Kīlauea décollement (e.g., Foster et al., 2013; Lin et al., 2020; Montgomery-Brown et al., 2011; Wolfe et al., 2007). Foster et al. (2013) relates the range of seismic events and subsequent slip to frictional variability along the décollement, which appears consistent with our slip distribution pattern. For example, although we see southward slip along the western edge of the décollement prior to the 1975 earthquake, our model requires little to no slip near the epicenter where slip nucleated, consistent with this portion of the décollement being locked and accumulating stress leading up to the rupture.

For the solutions plotted in Figures 9 and 10, the average southward slip rate prior to the 1975 Kalapana earthquake is 10 cm/yr, while after the rupture it drops to 4 cm/yr. This lower magnitude of decollement slip is also confirmed by individual station time series analysis (Figure 11c) located at the coast and mid-elevation stations, in the Hilina fault system and Lower East Rift region. These results are consistent with previous investigations reporting stabilization along the south flank of Kīlauea following the 1975 earthquake, while maintaining continued extension of the region at lower rates than those prior to the M_w7.7 rupture. The reduced interseismic rate of 4 cm/yr may also be connected to the SSEs that have recently been observed on the Kīlauea fault plane (e.g., Brooks et al., 2008; Foster et al., 2013).

The most recent large magnitude earthquake was the 2018 M_w6.9 earthquake that occurred shortly after our last observation time period of 1976–2018. The 2018 epicenter also resides in the same region as the 1975 Kalapana and other large earthquakes, where our 1976–2018 model resolves minimal to no slip along Kīlauea's décollement plane, just northeast of the region prone to SSEs (Foster et al., 2013; Liu et al., 2018) where we do resolve slip (see Figure 9c). Unlike the 1975 Kalapana earthquake, the 2018 rupture occurred during a major volcanic eruption involving Kīlauea's summit and East Rift Zone (Neal et al., 2019), and the earthquake was likely triggered by magmatic intrusions within the East Rift Zone (Patrick et al., 2020).

Notably, we see slip maintained west of Kīlauea's summit, and a general migration of higher magnitude slip eastward along Kīlauea's decollement and north of the Kalapana and Leilani Estate epicenters for the 42-year modern data set (1976–2018). However, Montgomery-Brown et al. (2011) report westward migration of slip along the décollement following the June 2007 East Rift Zone intrusion. Our slip patterns differ from those of Montgomery-Brown et al. (2011) and other studies that focus on smaller time periods or specific volcanic and/or seismic events (e.g., Hooper et al., 2002; Miklius et al., 2005; Owen, Segall, Lisowski, Miklius, Murray, et al., 2000; Owen, Segall, Lisowski, Miklius, Denlinger, & Sako, 2000). That is to be expected as we have focused here on longer time scales and parsimonious combinations of sources for the range of magmatic and seismic events.

5.2. Stress Changes From 1896 to 2018 Based on Modeled Deformation

Earthquakes and magmatic intrusions throughout the Mauna Loa and Kīlauea regions of Hawai'i have been linked to areas of increased stress that load a particular fault or rift until failure (e.g., Cayol et al., 2000; Crosson &

Endo, 1981; Gillard, Wyss, & Okubo, 1996; Neal et al., 2019; Thurber & Gripp, 1988; Varugu & Amelung, 2021; Walter & Amelung, 2006). Inferring the stress fields from deformation observations can therefore provide additional geophysical insight into the loading conditions of events leading up to and following earthquakes and intrusions. Taking our modeled source solutions for each time period, which includes the patched slip/opening along fault planes and the magmatic point source deformation, we use the Coulomb 3.3 software (Lin & Stein, 2004; Toda et al., 2011) to resolve stress changes along the Kīlauea décollement and the East Rift Zone (Figure 12 and Figures S3–S5 in Supporting Information S1) for our three time periods. Shear stress change ($\Delta\tau_\beta$) and normal stress change ($\Delta\sigma_n$) are resolved onto planes of specified orientation (i.e., receiver fault orientations) and combined with an assumed coefficient of effective friction to evaluate Coulomb failure stress change ($\Delta\sigma_c$, Equation 7). Effective friction includes the impact of pore-pressure on the frictional strength, and we have chosen the value $\mu = 0.4$ (e.g., King et al., 1994, and as recommended by the Coulomb 3.3 software package) as an appropriate default. Although previous work has shown that friction likely varies spatially across the décollement (Foster et al., 2013) and will also vary temporally, changes in μ have been found to have only a minor impact on this type of stress analysis (e.g., King et al., 1994).

$$\Delta\sigma_c = (\Delta\tau_\beta + \mu\Delta\sigma_n) \tag{7}$$

Here we assume increasing seaward shear (updip along the décollement) and decreasing normal compressive stress changes to be positive. Coulomb stress change is regularly used to evaluate earthquake triggering (e.g., Chen et al., 2019; King et al., 1994), where a positive stress change can promote fault rupture. Likewise, the decreased (positive change) and increased normal compressive (negative change) stress across the rift zones can promote or inhibit magmatic intrusions (Amelung et al., 2007; Walter & Amelung, 2006). The stress changes at depth throughout time are calculated along profiles intersecting key geologic features, such as Kīlauea's summit and décollement, the East Rift Zone, and the epicenters of the 1975 M_w7.7 Kalapana and 2018 M_w6.9 earthquake, and then compared to observed seismicity.

We examine the changes in stress over time in terms of: (a) *Coulomb stress changes along Kilauea's decollement,* where $\Delta\sigma_c$ is calculated for a receiver fault geometry prescribed to be that of the Kīlauea décollement fault plane in Table 1 (plotted on the left side of Figure S3 in Supporting Information S1); and (b) N*ormal stress changes along Kilauea's East Rift Zone* where the normal stresses, $\Delta\sigma_n$, are resolved across a receiver fault geometry prescribed to be that of the East Rift in Table 1 (are plotted on the right side of Figure S3 in Supporting Information S1). For visual reference, simplified representations of stress change from homogeneous slip along geometries consistent with Kilauea's decollement and the East Rift Zone are provided at the top of Figure S3 in Supporting Information S1 (stress changes along the decollement and rift zones resulting only from Kīlauea décollement displacement are shown in Figures S4 and S5 in Supporting Information S1). Figure 12 depicts a simplified schematic of the resulting Coulomb and normal stress changes over time from our modeled deformation.

5.2.1. 1896–1974 Stress Changes

Prior to the 1975 Kalapana earthquake (1896–1974), heterogeneous Coulomb stress changes appear along both the Kīlauea décollement and East Rift Zone (Figure 12a; Figures S3a and S3b in Supporting Information S1) as a result of interseismic slip (and locked patches) along both Mauna Loa and Kilauea decollements, rift zone deformation, and magmatic inflation at Kīlauea and deflation at Mauna Loa, Mauna Ulu, and Pu‘u ‘Ō‘ō. At depth, along the western side of the Kīlauea décollement (Figure S3a in Supporting Information S1, profile A-A′), slip on the decollement (Figure 9a) coincides with reduced Coulomb stress and increased Coulomb stress occurs surrounding slipping regionsClusters of seismicity coincide with the depths of both décollements. The stress changes surrounding the pending 1975 Kalapana earthquake epicenter (Figure 12; Figure S3a in Supporting Information S1, profile B-B′) reveal a small positive shear stress lobe that intersects the décollement plane. The increase in Coulomb stress here is associated with expansion of the East Rift (see Figure S4 in Supporting Information S1 for stress caused from all active sources vs. just the Kīlauea décollement for the 1896–1974 time period). A large zone of decreased Coulomb stress also occurs updip and offshore from the 1975 Kalapana earthquake, where southward slip was resolved by our deformation model (Figure 9a).

Along the East Rift Zone (Figure 12; Figure S3b in Supporting Information S1), a strong decrease in normal compressive stress is found at shallow depths Kīlauea (Southwest and East) Rift Zones. \In the East Rift zone increased compressive normal stress is seen at 3–5 km depths as a response to dike intrusions. Above and below this zone we find decreased compressive stress promoting shallow intrusion. This is similar to the example in the top right panel of Figure S3 in Supporting Information S1. Both the Southwest and East Rift Zones coincide with large clusters of earthquakes at depth, as seismic activity is heavily linked to magmatic intrusions throughout the Kīlauea region.

The increased Coulomb stress along the Kīlauea décollement and around the location of the 1975 earthquake epicenter portrays conditions favorable for decollement rupture leading up to the 1975 Kalapana earthquake. This is consistent with studies that indicate the 1975 earthquake was most likely caused by a combination of pressure changes from magmatic intrusions within the rift zones at depth and from Kīlauea south flank deformations caused by volcanic spreading (e.g., Swanson et al., 1976) and gravitational instability (e.g., Yin & Kelty, 2000). Both driving mechanisms are mechanically feasible and are consistent with our resultant stress field.

5.2.2. 1975 Stress Changes

Slip from the 1975 Kalapana earthquake (Figure 9b) generates stress changes (Figure 12b; Figures S3c and S3d in Supporting Information S1) an order of magnitude greater than the time period prior. The decrease in Coulomb stress along the decollement is a result of meters of both horizontal and vertical slip from the M_w7.7 earthquake (Nettles & Ekström, 2004).

Resolved normal stress changes (Figure S3d in Supporting Information S1) show a broad decrease in compressive normal stress along the East Rift Zone as a result of decollement slip from the Kalapana earthquake. This decrease may have increased the possibility of magmatic intrusions there. This decrease also overlaps with a cluster of earthquakes at depth. Despite these large normal stress changes, our model source analysis did not require any opening along the East Rift Zone in order to reproduce the observed displacements, indicating that the rift-normal stress state remained compressional.

5.2.3. 1976–2018 Stress Changes

After the 1975 Kalapana earthquake, low-magnitude Coulomb stress reduction is apparent over much of the decollement (Figure 12c and Figure S3e in Supporting Information S1), consistent with low rate but spatially extensive slip along the fault planes and decreased volume change for Kīlauea's magma chamber (Table 2). We note the zone of reduced stress near the coastline of profile A-A′ along the decollement (Figure S3e in Supporting Information S1), which coincides with the region identified as hosting SSEs (Foster et al., 2013). A similar Coulomb stress change pattern along the décollement was also found by Brooks et al. (2008) coinciding with SSEs.

We also find decreased shear stress along the décollement coinciding with the epicenter of the future 2018 M_w6.9 earthquake (Figure 12c and Figure S3e in Supporting Information S1, profile B-B′). While decreased shear stress near the 2018 earthquake epicenter (rupture depth 5.7 km (Neal et al., 2019)) would not encourage future fault failure here, the decreased compressive stress seen along the East Rift Zone (Figure 12c; Figure S3f in Supporting Information S1) could promote favorable conditions for magmatic intrusions within the area. Intrusions into the East Rift Zone during the 2018 eruption are thought to be the catalyst for the 2018 earthquake (Chen et al., 2019; Neal et al., 2019) by increasing the shear stress on the décollement (Patrick et al., 2020).

6. Conclusions

We assimilated deformation observations from several types of geodetic data over the past 122 years within the Mauna Loa and Kīlauea regions of Hawai'i Island. A range of deformation sources were investigated to reproduce observations using an analytical deformation model that reflects three main modes of dislocation: (a) low-angle décollement fault planes that slip southward and underly the Mauna Loa and Kīlauea volcanoes, (b) opening and contracting magmatic rift zones and interwoven fault systems, and (c) magmatic sources that can inflate or deflate as a response to the movement of magma. Using a 5-fold cross-validation technique, we established an optimal combination of tectonic and magmatic deformation sources during three distinct time periods surrounding the

1975 M_w7.7 Kalapana earthquake: before (1986–1974), during (1975), and after (1976–2018). Our study developed a robust analytical model to explore both long (1896–1974 and 1976–2018) and short (1975, encompassing the Kalapana earthquake) timescales of deformation and stress for a variety of geodetic observations, as well as a user-friendly compilation of data. We calculated Coulomb and normal stress changes resulting from the modeled deformation over the three time periods.

Our conclusions are: (a) Multiple sources are needed to reproduce the 122 years of observations, with the most needed for the period prior to the 1975 Kalapana earthquake, and these sources vary with time. (b) Complex and high magnitude slip rates occurred throughout the region before the 1975 M_w7.7 Kalapana earthquake; despite this high rate of motion of Kīlauea's south flank, it still experienced compression as reported by previous studies (e.g., Swanson et al., 1976; Thurber & Gripp, 1988). In contrast, slip complexity and magnitude are reduced throughout the region after the 1975 rupture, where the average slip along the Kīlauea décollement decreased from 10 to 4 cm/yr. This regional stabilization is consistent with previous studies (e.g., Day et al., 2005; Delaney et al., 1998). (c) We find increased Coulomb stress along the Kīlauea décollement and decreased normal compressive stresses along the East Rift Zone before 1975, promoting favorable conditions for both rifting and magmatic intrusion leading up to the Kalapana earthquake. Both mechanisms have been suggested as plausible triggers of the 1975 earthquake. (d) Variable Coulomb stress changes along Kīlauea's décollement after 1975 do not suggest a strong promotion of decollement failure, but large decreases in compressive stress are noted along the East Rift Zone. Therefore, subsequent seismic events (such as the 2018 M_w6.9 earthquake) are more likely to have been triggered by East Rift Zone intrusions favored by this stress change. (e) The diverse patterns and magnitude of slip and stress throughout all three time periods show how deformation changed with time and amongst deformation sources. These varied slip patterns further promote the mechanical plausibility of diverse seismic and magmatic events produced by the same deformation source(s). Future analyses would benefit from a search for frictional properties, especially along the Kīlauea fault plane.

Data Availability Statement

The EDM and leveling data are available at http://pgf.soest.hawaii.edu/EXTDATA/public as are the velocities for the continuous GNSS sites used here. The 1990–1996 campaign GNSS data set can be found within Owen, Segall, Lisowski, Miklius, Murray, et al. (2000), the 1896–1970 triangulation and trilateration were provided within Swanson et al. (1976), and the 2000–2004 vertical displacements obtained from offshore pressure sensors are reported in Phillips et al. (2008). The Centroid-Moment-Tensor (CMT) solutions for the 2018 M_w6.9, 1989 south flank M_w6.1, and 1983 Kaoiki M_w6.6 earthquakes are available at www.globalcmt.org (Dziewonski et al., 1981; Ekström et al., 2012). The CMT solution for the 1975 Kalapana M_w7.7 earthquake was provided by Nettles and Ekström (2004). The seismicity data from 1986 to 2018 was provided by Matoza et al. (2021), from 1960 to 2016 by NCEDC (2014), and from 1933 to 1959 by Klein and Wright (2000). Elevation and bathymetry data used throughout this study are available for download at http://www.soest.hawaii.edu/hmrg/multibeam/index.php. Supporting Information includes Figures S1–S5 in Supporting Information S1. The data files used in this paper are available at Yong et al. (2024).

Acknowledgments

We thank Emily Montgomery-Brown for guiding us with her expertise and suggestions throughout this project, and A. Miklius, I. Johanson and the HVO staff for collecting and providing the 1970–1995 electronic distance measurements, 1963–2012 leveling, and 1996–2018 continuous GNSS data sets used throughout this study. We also thank the Hawaii Center for Volcanology (http://www.soest.hawaii.edu/GG/hcv.html) and Ken Rubin at UH Mānoa for its maintenance, where we obtained details from many major historical magmatic events that occurred within Kīlauea's and Mauna Loa's volcanic systems. This work was supported by the National Science Foundation (NSF 1824114) awarded to PIs J.H. Foster and it is SOEST Contribution #11816.

References

Amelung, F., Yun, S.-H., Walter, T. R., Segall, P., & Kim, S.-W. (2007). Stress control of deep rift intrusion at Mauna Loa Volcano, Hawaii. *Science*, *316*(5827), 1026–1030. https://doi.org/10.1126/science.1140035

Arnadottir, T., Segall, P., & Delaney, P. (1991). A fault model for the 1989 Kilauea South Flank Earthquake from leveling and seismic data. *Geophysical Research Letters*, *18*(12), 2217–2220. https://doi.org/10.1029/91GL0269

Atkinson, G. M. (2010). Ground-motion prediction equations for Hawaii from a referenced empirical approach. *Bulletin of the Seismological Society of America*, *100*(2), 751–761. https://doi.org/10.1785/0120090098

Baker, S., & Amelung, F. (2015). Pressurized magma reservoir within the east rift zone of Kīlauea Volcano, Hawai'i: Evidence for relaxed stress changes from the 1975 Kalapana earthquake. *Geophysical Research Letters*, *42*(6), 1758–1765. https://doi.org/10.1002/2015GL063161

Borgia, A., Delaney, P. T., & Denlinger, R. P. (2000). Spreading volcanoes. *Annual Review of Earth and Planetary Sciences*, *28*(1), 539–570. https://doi.org/10.1146/annurev.earth.28.1.539

Brooks, B. A., Foster, J., Sandwell, D., Wolfe, C. J., Okubo, P., Poland, M., & Myer, D. (2008). Magmatically triggered slow slip at Kilauea Volcano, Hawaii. *Science*, *321*(5893), 1177. https://doi.org/10.1126/science.1159007

Byrnes, J. M., Ramsey, M. S., & Crown, D. A. (2004). Surface unit characterization of the Mauna Ulu flow field, Kilauea Volcano, Hawai'i, using integrated field and remote sensing analyses. *Journal of Volcanology and Geothermal Research*, *135*(1–2), 169–193. https://doi.org/10.1016/j.jvolgeores.2003.12.016

Cannon, E. C., Burgmann, R., & Owen, S. E. (2001). Shallow normal faulting and block rotation associated with the 1975 Kalapana earthquake, Kilauea Volcano, Hawaii. *Bulletin of the Seismological Society of America*, *91*(6), 1553–1562. https://doi.org/10.1785/0120000072

Cayol, V., & Cornet, F. H. (1998). Effects of topography on the interpretation of the deformation field of prominent volcanoes—Application to Etna. *Geophysical Research Letters*, *25*(11), 1979–1982. https://doi.org/10.1029/98gl51512

Cayol, V., Dieterich, J. H., Okamura, A. T., & Miklius, A. (2000). High magma storage rates before the 1983 eruption of Kilauea, Hawaii. *Science*, *288*(5475), 2343–2346. https://doi.org/10.1126/science.288.5475.2343

Cervelli, P., Segall, P., Johnson, K., Lisowski, M., & Miklius, A. (2002). Sudden aseismic fault slip on the south flank of Kilauea Volcano. *Nature*, *415*(6875), 1014–1018. https://doi.org/10.1038/4151014a

Chen, K., Smith, J. D., Avouac, J., Liu, Z., Song, Y. T., & Gualandi, A. (2019). Triggering of the Mw 7.2 Hawaii earthquake of 4 May 2018 by a dike intrusion. *Geophysical Research Letters*, *46*(5), 2503–2510. https://doi.org/10.1029/2018GL081428

Coles, S. (2001). *An introduction to statistical modeling of extreme values* (4th ed.). Springer.

Crosson, R. S., & Endo, E. T. (1981). Focal mechanisms of earthquakes related to the 29 November 1975 Kalapana, Hawaii Earthquake: The effect of structure models. *Bulletin of the Seismological Society of America*, *71*(3), 713–729. https://doi.org/10.1785/BSSA0710030713

Day, S. J., Watts, P., Grilli, S. T., & Kirby, J. T. (2005). Mechanical models of the 1975 Kalapana, Hawaii earthquake and tsunami. *Marine Geology*, *215*(1–2), 59–92. https://doi.org/10.1016/j.margeo.2004.11.008

Decker, R. W., Okamura, A. T., Miklius, A., & Poland, M. P. (2008). Evolution of deformation studies on active Hawaiian volcanoes, *U.S. Geological Survey Scientific Investigations Report 2008-5090* (p. 23).

Delaney, P. T., & Denlinger, R. P. (1999). Stabilization of volcanic flanks by dike intrusion: An example from Kilauea. *Bulletin of Volcanology*, *61*(6), 356–362. https://doi.org/10.1007/s004450050278

Delaney, P. T., Denlinger, R. P., Lisowski, M., Miklius, A., Okubo, P. G., Okamura, A. T., & Sako, M. K. (1998). Volcanic spreading at Kilauea, 1976–1996. *Journal of Geophysical Research*, *103*(B8), 18003–18023. https://doi.org/10.1029/98JB01665

Delaney, P. T., Wyss, M., Lipman, P. W., & Okamura, A. T. (1992). Comment [on "Precursors to the Kalapana M_w = 7.2 Earthquake" by Max Wyss, F. W. Klein, and Arch C. Johnston]. *Journal of Geophysical Research*, *97*(B4), 4839–4841. https://doi.org/10.1029/91JB02924

Denlinger, R. P., & Okubo, P. (1995). Structure of the mobile south flank of Kilauea Volcano, Hawaii. *Journal of Geophysical Research*, *100*(B12), 24499–24507. https://doi.org/10.1029/95JB01479

Dziewonski, A. M., Chou, T.-A., & Woodhouse, J. H. (1981). Determination of earthquake source parameters from waveform data for studies of global and regional seismicity [Dataset]. *Journal of Geophysical Research*, *86*(B4), 2825–2852. https://doi.org/10.1029/JB086iB04p02825

Ekström, G., Nettles, M., & Dziewoński, A. M. (2012). The global CMT project 2004–2010: Centroid-moment tensors for 13,017 earthquakes [Dataset]. *Physics of the Earth and Planetary Interiors*, *200–201*, 1–9. https://doi.org/10.1016/j.pepi.2012.04.002

Foster, J. H., Lowry, A. R., & Brooks, B. A. (2013). Fault frictional parameters and material properties revealed by slow slip events at Kilauea volcano, Hawai'i. *Geophysical Research Letters*, *40*(23), 6059–6063. https://doi.org/10.1002/2013GL058234

Garcia, M. O., Pietruszka, A. J., Norman, M. D., & Rhodes, J. M. (2021). Kīlauea's Pu'u 'Ō'ō Eruption (1983–2018): A synthesis of magmatic processes during a prolonged basaltic event. *Chemical Geology*, *581*, 120391. https://doi.org/10.1016/j.chemgeo.2021.120391

Gillard, D., Rubin, A. M., & Okubo, P. (1996). Highly concentrated seismicity caused by deformation of Kilauea's deep magma system. *Nature*, *384*(6607), 343–346. https://doi.org/10.1038/384343a0

Gillard, D., Wyss, M., & Okubo, P. (1996). Type of faulting and orientation of stress and strain as a function of space and time in Kilauea's south flank, Hawaii. *Journal of Geophysical Research*, *101*(B7), 16025–16042. https://doi.org/10.1029/96JB00651

Got, J.-L., Fréchet, J., & Klein, F. W. (1994). Deep fault plane geometry inferred from multiplet relative relocation beneath the south flank of Kilauea. *Journal of Geophysical Research*, *99*(B8), 15375–15386. https://doi.org/10.1029/94JB00577

Got, J.-L., & Okubo, P. (2003). New insights into Kilauea's volcano dynamics brought by large-scale relative relocation of microearthquakes. *Journal of Geophysical Research*, *108*(B7), 2337. https://doi.org/10.1029/2002JB002060

Hanatani, R. Y. (1987). Permanent-glass EDM measurements on Kilauea, Hawaii, from June 6, 1979, to September 23, 1987, *U.S. Geological Survey Open-File Report 87-202* (p. 97).

Hooper, A., Segall, P., Johnson, K., & Rubinstein, J. (2002). Reconciling seismic and geodetic models of the 1989 Kilauea south flank earthquake. *Geophysical Research Letters*, *29*(22). 19-1–19-4. https://doi.org/10.1029/2002GL016156

James, G., Witten, D., Hastie, T., & Tibshirani, R. (2013). *An introduction to statistical learning: With applications in R* (1st ed.). Springer Texts in Statistics.

Johnson, D. J. (1987). Elastic and inelastic magma storage at Kilauea volcano. *US Geological Survey Professional Paper*, *1350*, 1297–1306.

Johnson, D. J. (1992). Dynamics of magma storage in the summit reservoir of Kilauea Volcano, Hawaii. *Journal of Geophysical Research*, *97*(B2), 1807–1820. https://doi.org/10.1029/91jb02839

King, G. C. P., Stein, R. S., & Lin, J. (1994). Static stress changes and the triggering of earthquakes. *Bulletin of the Seismological Society of America*, *84*(3), 935–953. https://doi.org/10.1785/BSSA0840030935

Klein, F. W., & Wright, T. L. (2000). Catalog of Hawaiian earthquakes, 1823–1959 [Dataset]. *U.S. Geological Survey Professional Paper 1623*, 90. https://doi.org/10.3133/pp1623

Lin, J., & Stein, R. S. (2004). Stress triggering in thrust and subduction earthquakes and stress interaction between the southern San Andreas and nearby thrust and strike-slip faults. *Journal of Geophysical Research*, *109*(B2), B02303. https://doi.org/10.1029/2003JB002607

Lin, J.-T., Aslam, K. S., Thomas, A. M., & Melgar, D. (2020). Overlapping regions of coseismic and transient slow slip on the Hawaiian décollement. *Earth and Planetary Science Letters*, *544*, 116353. https://doi.org/10.1016/j.epsl.2020.116353

Lipman, P. W., Lockwood, J. P., Okamura, R. T., Swanson, D. A., & Yamashita, K. M. (1985). *Ground deformation associated with the 1975 magnitude-7.2 earthquake and resulting changes in activity of Kilauea Volcano, Hawaii* (Vol. 1276). US Government Printing Office. Retrieved from https://pubs.usgs.gov/pp/1276/report.pdf

Liu, C., Lay, T., & Xiong, X. (2018). Rupture in the 4 May 2018 Mw 6.9 earthquake seaward of the Kilauea East Rift Zone fissure eruption in Hawaii. *Geophysical Research Letters*, *45*(18), 9508–9515. https://doi.org/10.1029/2018GL079349

Lockwood, J. P., Tillings, R. I., Holcomb, F. K., Okamura, A. T., Petersen, D. W., & Peterson, D. W. (1999). *Magma migration and resupply during the 1974 summit eruptions of Kīlauea Volcano, Hawai'i* (Vol. 1613). US Department of the Interior, US Geological Survey; Information Services. Retrieved from https://pubs.usgs.gov/pp/pp1613/pp1613.pdf

Ma, K.-F., Kanamori, H., & Satake, K. (1999). Mechanism of the 1975 Kalapana, Hawaii, earthquake inferred from tsunami data. *Journal of Geophysical Research*, *104*(B6), 13153–13167. https://doi.org/10.1029/1999JB900073

Matoza, R. S., Okubo, P. G., & Shearer, P. M. (2021). Comprehensive high-precision relocation of seismicity on the Island of Hawai'i 1986–2018 [Dataset]. *Earth and Space Science*, *8*(1), e2020EA001253. https://doi.org/10.1029/2020EA001253

McNamara, D. E., Wolin, E., Powers, P. M., Shumway, A. M., Moschetti, M. P., Rekoske, J., et al. (2020). Evaluation of ground-motion models for U.S. Geological Survey seismic hazard forecasts: Hawaii tectonic earthquakes and volcanic eruptions. *Bulletin of the Seismological Society of America*, *110*(2), 666–688. https://doi.org/10.1785/0120180336

Miklius, A., Cervelli, P., Sako, M., Lisowski, M., Owen, S., Segal, P., et al. (2005). Global positioning system measurements on the Island of Hawai`i: 1997 through 2004. *US Geological Survey Open File Report*, 48.

Mogi, K. (1958). Relations between the eruptions of various volcanoes and the deformations of the ground surfaces around them. *Bulletin of the Earthquake Research Institute*, *36*, 99–134.

Montgomery-Brown, E. K., Segall, P., & Miklius, A. (2009). Kilauea slow slip events: Identification, source inversions, and relation to seismicity. *Journal of Geophysical Research*, *114*(B6), B00A03. https://doi.org/10.1029/2008JB006074

Montgomery-Brown, E. K., Sinnett, D. K., Larson, K. M., Poland, M. P., Segall, P., & Miklius, A. (2011). Spatiotemporal evolution of dike opening and décollement slip at Kīlauea Volcano, Hawai'i. *Journal of Geophysical Research*, *116*(B3), B03401. https://doi.org/10.1029/2010JB007762

Montgomery-Brown, E. K., Sinnett, D. K., Poland, M., Segall, P., Orr, T., Zebker, H., & Miklius, A. (2010). Geodetic evidence for en echelon dike emplacement and concurrent slow slip during the June 2007 intrusion and eruption at Kīlauea volcano, Hawaii. *Journal of Geophysical Research*, *115*(B7), B07405. https://doi.org/10.1029/2009JB006658

Morgan, J. K. (2006). Volcanotectonic interactions between Mauna Loa and Kilauea: Insights from 2-D discrete element simulations. *Journal of Volcanology and Geothermal Research*, *151*(1–3), 109–131. https://doi.org/10.1016/j.jvolgeores.2005.07.025

Morgan, J. K., Moore, G. F., & Clague, D. A. (2003). Slope failure and volcanic spreading along the submarine south flank of Kilauea volcano, Hawaii. *Journal of Geophysical Research*, *108*(B9), 2415. https://doi.org/10.1029/2003JB002411

Morgan, J. K., Moore, G. F., Hills, D. J., & Leslie, S. (2000). Overthrusting and sediment accretion along Kilauea's mobile south flank, Hawaii: Evidence for volcanic spreading from marine seismic reflection data. *Geology*, *28*(7), 667–670. https://doi.org/10.1130/0091-7613(2000)028<0667:oasaak>2.3.co;2

NCEDC. (2014). 1960–2016 Hawai'i Earthquake Catalog Dataset]. *Northern California Earthquake Data Center, UC Berkeley Seismological Laboratory*. https://doi.org/10.7932/NCEDC

Neal, C. A., Brantley, S. R., Antolik, L., Babb, J. L., Burgess, M., Calles, K., et al. (2019). The 2018 rift eruption and summit collapse of Kīlauea Volcano. *Science*, *363*(6425), 367–374. https://doi.org/10.1126/science.aav7046

Nettles, M., & Ekström, G. (2004). Long-period source characteristics of the 1975 Kalapana, Hawaii, Earthquake [Dataset]. *Bulletin of the Seismological Society of America*, *94*(2), 422–429. https://doi.org/10.1785/0120030090

Okada, Y. (1985). Surface deformation due to shear and tensile faults in a half-space. *Bulletin of the Seismological Society of America*, *74*(4), 1135–1154. https://doi.org/10.1785/BSSA0750041135

Okubo, P. G., Benz, M., & Chouet, B. A. (1997). Imaging the crustal magma sources beneath Mauna Loa and Kilauea volcanoes, Hawaii. *Geology*, *25*(10), 867–870. https://doi.org/10.1130/0091-7613(1997)025<0867:ITCMSB>2.3.CO;2

Owen, S., Segall, P., Lisowski, M., Miklius, A., Denlinger, R., & Sako, M. (2000). Rapid deformation of Kilauea Volcano: Global Positioning System measurements between 1990 and 1996. *Journal of Geophysical Research*, *105*(B8), 18983–18998. https://doi.org/10.1029/2000JB900109

Owen, S., Segall, P., Lisowski, M., Miklius, A., Murray, M., Bevis, M., & Foster, J. (2000). 1997 eruptive event on Kilauea Volcano, Hawaii, as monitored by continuous GPS [Dataset]. *Geophysical Research Letters*, *27*(17), 2757–2760. https://doi.org/10.1029/1999GL008454

Patrick, M., Johanson, I., Shea, T., & Waite, G. (2020). The historic events at Kīlauea Volcano in 2018: Summit collapse, rift zone eruption, and Mw 6.9 earthquake: Preface to the special issue. *Bulletin of Volcanology*, *82*(6), 46. https://doi.org/10.1007/s00445-020-01377-5

Phillips, K. A., Chadwell, C. D., & Hildebrand, J. A. (2008). Vertical deformation measurements on the submerged south flank of Kīlauea volcano, Hawai'i reveal seafloor motion associated with volcanic collapse [Dataset]. *Journal of Geophysical Research*, *113*(B5), B05106. https://doi.org/10.1029/2007JB005124

Segall, P., Cervelli, P., Owen, S., Lisowski, M., & Miklius, A. (2001). Constraints on dike propagation from continuous GPS measurements. *Journal of Geophysical Research*, *106*(B9), 19301–19317. https://doi.org/10.1029/2001JB000229

Shirzaei, M., Walter, T. R., & Bürgmann, R. (2013). Coupling of Hawaiian volcanoes only during overpressure condition: Coupling of Hawaiian Volcanoes. *Geophysical Research Letters*, *40*(10), 1994–1999. https://doi.org/10.1002/grl.50470

Swanson, D. A. (1973). Pahoehoe flows from the 1969–1971 Mauna Ulu eruption, Kilauea volcano, Hawaii. *GSA Bulletin*, *84*(2), 615–626. https://doi.org/10.1130/0016-7606(1973)84<615:PFFTMU>2.0.CO;2

Swanson, D. A., Duffield, W. A., & Fiske, R. S. (1976). Displacement of the south flank of Kilauea Volcano: The result of forceful intrusion of magma into the rift zones. *US Geological Survey Professional Paper*, *963*, 39.

Thurber, C. H., & Gripp, A. E. (1988). Flexure and seismicity beneath the south flank of Kilauea Volcano and tectonic implications. *Journal of Geophysical Research*, *93*(B5), 4271–4278. https://doi.org/10.1029/JB093iB05p04271

Toda, S., Stein, R. S., Sevilgen, V., & Lin, J. (2011). Coulomb 3.3 graphic-rich deformation and stress-change software for earthquake, tectonic, and volcano research and teaching – User guide [Software]. *US Geological Survey Open-File Report*. https://doi.org/10.3133/OFR20111060

Varugu, B., & Amelung, F. (2021). Southward growth of Mauna Loa's dike-like magma body driven by topographic stress. *Scientific Reports*, *11*(1), 9816. https://doi.org/10.1038/s41598-021-89203-6

Walter, T. R., & Amelung, F. (2006). Volcano-earthquake interaction at Mauna Loa volcano, Hawaii: Stress Transfer at Mauna Loa. *Journal of Geophysical Research*, *111*(B5), B05204. https://doi.org/10.1029/2005JB003861

Wolfe, C. J., Brooks, B. A., Foster, J. H., & Okubo, P. G. (2007). Microearthquake streaks and seismicity triggered by slow earthquakes on the mobile south flank of Kilauea Volcano, Hawai'i. *Geophysical Research Letters*, *34*(23). https://doi.org/10.1029/2007GL031625

Wright, T. L., & Klein, F. W. (2014). *Two hundred years of magma transport and storage at Kīlauea Volcano, Hawai'i, 1790–2008* (Vol. 1806). US Geological Survey. Retrieved from https://pubs.usgs.gov/pp/1806/pdf/pp1806_report.pdf

Wu, W., Hu, J., Liu, J., Li, Z., Zhu, J., Xu, B., et al. (2021). Derivation of high-quality three-dimensional surface deformation velocities through multi-source point cloud fusion: Application to Kīlauea volcano. *International Journal of Applied Earth Observation and Geoinformation*, *95*, 102270. https://doi.org/10.1016/j.jag.2020.102270

Wyss, M. (1988). A proposed source model for the Great Kau, Hawaii, Earthquake of 1868. *Bulletin of the Seismological Society of America*, *78*(4), 1450–1462. https://doi.org/10.1785/BSSA0780041450

Yin, A., & Kelty, T. K. (2000). An elastic wedge model for the development of coeval normal and thrust faulting in the Mauna Loa-Kilauea rift system in Hawaii. *Journal of Geophysical Research*, *105*(B11), 25909–25925. https://doi.org/10.1029/2000JB900247

Yong, L. W., Foster, J. H., Smith-Konter, B. R., & Frazer, L. N. (2024). A century of deformation and stress change on Kīlauea's décollement. [Dataset]. *Journal of Geophysical Research: Solid Earth*. https://doi.org/10.1029/2024JB028714